Epimutations driven by RNAi or heterochromatin evoke transient antimicrobial drug resistance in fungi

Ye-Eun Son[1], Carlos Pérez-Arques[1], and Joseph Heitman[1*]

[1] *Department of Molecular Genetics and Microbiology, Duke University Medical Center, Durham, NC 27710, USA*

[*] **Corresponding Author:**

213 Research Drive, Durham, NC 27710, USA

Tel: 919-684-2824, Fax: 919-684-2790

Email: heitm001@duke.edu

Keywords: *Mucor*, Epigenetic resistance, RNA silencing, Histone modification, *In vivo* stability

Abstract

Antimicrobial resistance (AMR) is a global health threat emerging through microbe adaptation, driven by genetic variation, genome plasticity or epigenetic process. In this study, we investigated how the *Mucor circinelloides* species complex adapts to the antifungal natural product FK506, which binds to FKBP12 and inhibits calcineurin-dependent hyphal growth. In *Mucor bainieri*, most FK506-resistant isolates (90%) were found to be unstable and transient, readily reverting to drug sensitivity when passaged without drug, and with no associated DNA mutations. In half of the isolates (50%), FK506-resistance was conferred by RNAi-dependent epimutation in which small interfering RNAs (siRNAs) silenced the *fkbA* encoding FKBP12 post-transcriptionally. In contrast, most of the remaining FK506-resistant isolates (40%) were found to have undergone heterochromatin-mediated silencing via H3K9 dimethylation, transcriptionally repressing *fkbA* and neighboring genes. In these heterochromatic epimutants, only minimal enrichment of siRNA to the *fkbA* locus was observed, but in three of the four examples, siRNA was significantly enriched at a locus distant from *fkbA*. A similar mechanism operates in *Mucor atramentarius*, where FK506 resistance was mediated by ectopic heterochromatin silencing *fkbA* and associated genes with siRNA spreading across the region. Heterochromatin-mediated *fkbA* epimutants exhibited stability during *in vivo* infection, suggesting epimutation could impact pathogenesis. These findings reveal that antifungal resistance arising through distinct, transient epimutation pathways involving RNAi or heterochromatin, highlighting adaptive AMR strategies employed by ubiquitous eukaryotic microbes.

45 **Introduction**

46 Fungi are ubiquitous eukaryotic organisms that occupy diverse ecological niches.
47 While many fungi contribute to food production, pharmaceutical development, and
48 biotechnology, others are pathogens capable of infecting a wide range of hosts including
49 humans [1]. The global burden of fungal infections has risen dramatically, now accounting
50 for an estimated two million deaths annually [2, 3]. Despite this growing threat, therapeutic
51 options remain limited due to a restricted antifungal arsenal, inadequate diagnostics, and
52 an alarming rise in antifungal resistance. The widespread use of antifungal agents in
53 agriculture and healthcare, combined with environmental pressures such as climate
54 change, has intensified selective pressure on fungal populations, driving the emergence
55 of fungal antimicrobial resistance (fAMR) [4-7].

56 Fungi employ both genetic and epigenetic strategies to adapt to antifungal stress
57 [8, 9]. Genetic changes include point mutations (missense/nonsense) and insertions and
58 deletions (indels) in drug target genes or drug transporter genes or their regulators, as
59 well as large-scale chromosomal alterations such as copy number variation and
60 aneuploidy. These changes confer resistance in several human fungal pathogens
61 including *Candida albicans*, *Cryptococcus neoformans*, *Aspergillus fumigatus*, and *Mucor*
62 *circinelloides* [10-13]. In contrast, epigenetic modifications enable non-Mendelian
63 inheritance of resistance without altering the underlying DNA sequence. These include
64 processes such as DNA methylation, RNA interference (RNAi), ectopic heterochromatin,
65 and DNA methylation [14].

66 In *Mucor circinelloides*, RNAi-dependent silencing of *fkbA*—which encodes
67 FKBP12, the cellular target of FK506 (tacrolimus)—confers transient FK506 resistance

68 that reverts in the absence of drug pressure [15]. RNAi-mediated silencing of *pyrF* or *pyrG*
69 prevents conversion of 5-fluoroorotic acid (5-FOA) into its toxic form, leading to transient
70 5-FOA resistance in *M. circinelloides* [16]. In addition, heterochromatin-driven gene
71 silencing has been implicated in stress adaptation. In *Schizosaccharomyces pombe*,
72 exposure to caffeine, an environmental stressor, selects for epimutations in which induces
73 the formation of histone 3 lysine 9 dimethylation (H3K9me2)-enriched heterochromatin
74 islands silence genes and promote survival without genetic mutation [17].

75 Mucormycosis is a life-threatening infection caused by Mucorales species
76 including *Mucor* and *Rhizopus* [18]. Spores enter the host via inhalation, traumatic injury,
77 or the rhino-orbital-cerebral route, often resulting in rapid dissemination, especially in
78 immunocompromised individuals with conditions such as diabetes mellitus, malignancy,
79 malnutrition, organ transplantation, or trauma [19, 20]. The mortality rate of mucormycosis
80 ranges from 50 to 90%, and incidence surged globally during the COVID-19 pandemic,
81 with over 3,000 deaths reported in India alone [21-23]. Recognizing the severity of
82 mucormycosis, the World Health Organization (WHO) recently designated Mucorales as
83 a high-priority fungal group in the Fungal Priority Pathogens List to drive research and
84 therapeutic development [9, 24]. Given both the severity and widespread incidence of
85 mucormycosis, a deeper understanding of intrinsic resistance and the potential for
86 acquired antifungal resistance is urgently needed to guide proper and efficient therapeutic
87 interventions.

88 The *Mucor circinelloides* complex (MCC) comprises at least 16 phylogenetic
89 species (PS), 7 of which have been isolated from clinical cases within Mucorales [25].
90 Prior studies in *M. lusitanicus* and *M. circinelloides* have identified both Mendelian and

91 epigenetic mechanisms of FK506 resistance, including RNAi-mediated silencing of *fkbA*
92 in the absence of mutations [15, 26-28]. However, whether such epigenetic regulation is
93 conserved across other MCC species—or whether alternative mechanisms exist—
94 remains unclear. In this study, we demonstrate that antifungal FK506 resistance in MCC
95 arises primarily through diverse genetic and epigenetic mechanisms, involving either
96 RNAi-mediated or heterochromatin-mediated epimutations that silence the *fkbA* gene
97 encoding the FK506 target FKBP12. Drug resistance conferred by both classes of
98 epimutation is unstable, and readily reverts following passage in the absence of drug in
99 contrast to mutations in the *fkbA* gene which are stably inherited even in the absence of
100 drug. Additionally, we demonstrate that FK506 resistance mediated by H3K9me2
101 heterochromatin is stably inherited after *in vivo* infection, providing new insights into the
102 durability and clinical relevance of epigenetic antifungal resistance.

Results

Screening of *Mucor circinelloides* species complex (MCC) reveals isolates resistant to FK506

Previous studies reported the phylogenetic classification of the MCC and divided the group into 16 phylogenetic species (PS) based on a polyphasic approach that included multi-locus sequence analyses, as well as morphological and physiological characterization [25]. RNAi-mediated epigenetic gene silencing has been shown to play a key role in FK506 resistance in *Mucor lusitanicus* (PS10) and *M. circinelloides* (PS14 and PS15) [15, 26]. In this study, we screened multiple species to isolate strains resistant to FK506, a calcineurin inhibitor known to prevent the dimorphic transition from yeast to hyphae, a process linked to virulence of *Mucor* [28], and rapamycin which also binds FKBP12 and the complex then inhibits TOR and blocks nutrient-stimulated growth [29]. Following the strategy outlined in **Fig 1A**, spores were collected and point-inoculated on YPD media with or without FK506, and the emergence of resistant colonies was monitored. Resistant colonies were observed in *Mucor janssenii* (PS1), *Mucor bainieri* (PS3), and *Mucor atramentarius* (PS6), as well as in the previously reported species *M. lusitanicus* (PS10) and *M. circinelloides* (PS14 and PS15) (**S1 Fig**).

To investigate the underlying mechanisms of resistance, we selected FK506-resistant isolates from *M. janssenii, M. bainieri,* and *M. atramentarius* for further analysis **(Fig 1B)**. The *fkbA* gene, three genes encoding calcineurin catalytic A (*cnaA*, *cnaB*, *cnaC*) subunits, and the calcineurin regulatory B subunit (*cnbR*) gene were amplified and analyzed by sequencing. As summarized (**Table 1**), four out of ten FK506-resistant isolates from *M. janssenii* exhibited large deletions spanning the *fkbA* locus. An additional

126 five isolates carried large insertions (~4 to 5 kb) in the *fkbA* promoter, nonsense mutations
127 within *fkbA* exons, or point mutations at splice sites. These *fkbA* mutants were cross-
128 resistant to rapamycin. In one isolate, a point mutation in the calcineurin A subunit gene
129 (*cnaA*) was associated with FK506 resistance but retained rapamycin susceptibility. Thus,
130 in *M. janssenii*, all ten isolates exhibited Mendelian mutations. In contrast, analysis of ten
131 FK506-resistant isolates from *M. bainieri* revealed only one isolate with a nonsense
132 mutation in *fkbA*, while the remaining nine exhibited no detectable sequence changes in
133 *fkbA*, or the genes encoding calcineurin A or B subunits, suggesting a possible epigenetic
134 regulation (**Table 1**). Similarly, in *M. atramentarius*, among ten FK506-resistant isolates,
135 three harbored nonsense mutations in *fkbA*, one contained a synonymous mutation, two
136 had splice-site point mutations, one had a start-loss mutation, and one had a point
137 mutation in the calcineurin B subunit (*cnbR*) (**Table 1**). Notably, two isolates showed no
138 genetic alterations in any of the sequenced genes.
139 In summary, these results indicate that all ten FK506-resistant isolates from *M.*
140 *janssenii* are Mendelian mutants. In *M. bainieri*, one isolate exhibited a Mendelian
141 mutation, while the remaining nine were identified as candidate epimutants. In *M.*
142 *atramentarius*, eight isolates carried Mendelian mutations, and two were classified as
143 candidate epimutants.
144
145 **FK506-resistant epimutants display reversible phenotypes characterized by**
146 **decreased levels of *fkbA* mRNA and FKBP12 protein expression**
147 For FK506-resistant isolates where no DNA sequence alterations were detected
148 in the FK506 target gene *fkbA* or the calcineurin genes, we hypothesized that resistance

149 might be regulated by epigenetic mechanisms. Because epimutations are typically
150 associated with reversible phenotypic plasticity [16], we tested whether FK506 resistance
151 would be lost after successive subculturing on drug-free medium. In fact, FK506
152 resistance was progressively lost following serial passages in the absence of selection
153 pressure (**Figs 2A, 2D** and **Table 2**). Resistant strains exhibited a hyphal morphology
154 and were capable of sporulation on FK506-containing media, whereas both wild-type (WT)
155 and revertant strains displayed a yeast-like morphology when exposed to FK506
156 treatment (**S2 Fig**). Additionally, in *M. bainieri*, phenotypic reversion occurred after an
157 average of 15.5 passages, whereas in *M. atramentarius*, reversion required
158 approximately 30 passages (**Figs 2A** and **2D**). Next, considering that epigenetic
159 alterations inhibit target gene expression without changes in the underlying nucleotide
160 sequence, we assayed *fkbA* transcript and FKBP12 protein levels. As shown in **Fig 2B**
161 and **2E**, the *fkbA* mRNA levels in all FK506-resistant strains were significantly reduced
162 compared to WT and were restored in all reverted strains. Consistently, FKBP12 protein
163 was undetectable in resistant strains and was restored in reverted epimutant isolates
164 (**Figs 2C** and **2F**). These results suggest that drug-resistant strains lacking genetic
165 changes represent epimutants, and that resistance reversion varies both between and
166 within species.
167

168 **Small RNAs confer FK506 resistance in *M. bainieri***

169 To determine which epigenetic mechanisms are involved in FK506 resistance in
170 *M. bainieri*, we first evaluated the potential role of 5mC DNA methylation. Whole-genome
171 sequencing data revealed the absence of canonical DNA 5-methylcytosine

172 methyltransferases (DNMT1, DIM-2, RID-1, DNMT4, and DNMT5), consistent with a
173 previous study (**S3A Fig**) [30]. Furthermore, 5mC analysis via Nanopore sequencing in
174 the two *Mucor* wild types detected no cytosine methylation, while a clear 5mC signal was
175 detected in a *Cryptococcus neoformans* clinical isolate with the same analysis pipeline
176 [31], suggesting that this mechanism is not involved in FK506 resistance (**S3B Fig**).

177 We next examined the involvement of RNAi by performing small RNA (sRNA)
178 sequencing. As shown in **Fig 3A** and **S4 Fig**, antisense small RNAs mapping to the *fkbA*
179 locus were detected in five of the nine FK506-resistant epimutants but were absent in WT
180 and revertant strains. The distribution pattern of sRNAs varied across epimutants. In
181 epimutants E5–E9, *fkbA*-specific sRNAs strongly accumulated to ~1,000 RPM, whereas
182 in WT and most revertants no reads were detected, with only a minimal signal (~1 RPM)
183 observed in E9 revertants (**Fig 3B**). The 5′ nucleotide of these sRNAs was predominantly
184 uracil (~82%; **Fig 3C**), and their length distribution peaked at 21–24 nucleotides (nt) (**Fig**
185 **3D**), consistent with the general features of Argonaute-loaded sRNAs [15, 32]. These
186 results indicate that the E5–E9 epimutants are RNAi-dependent epimutants, in which
187 FK506 resistance is mediated by *fkbA*-targeting antisense sRNAs that silence *fkbA* gene
188 expression.

189 In contrast to epimutants E5–E9, which exhibited abundant siRNAs mapping to
190 *fkbA*, epimutant isolates E1–E4 lacked detectable *fkbA*-targeting siRNAs (~1 RPM or less)
191 (**Figs 3A** and **Fig 3B**). However, E1–E3 displayed siRNAs mapping to neighboring genes
192 distant from *fkbA* (**S5 Fig**), with a strong 5′ uridine bias and predominant lengths of 21–
193 24 nt. For example, at *PS3_001333*, sRNAs reached ~2,595 RPM in epimutants E1-E3
194 but was largely absent in WT (0.15 RPM) and in revertants (1–1.6 RPM). Strikingly,

195 epimutant E4 lacked detectable siRNAs at both *fkbA* and its neighboring loci. To
196 determine whether epimutation spreading to *fkbA* from adjacent loci was associated with
197 transcriptional repression, we performed reverse transcription quantitative PCR (RT-
198 qPCR). As shown in **S5K Fig**, E1–E4 exhibited significant downregulation of genes
199 flanking *fkbA*. However, no significant changes were observed in the expression of *fkbA*-
200 neighboring genes in epimutants E7–E9. Meanwhile several genes (e.g., *PS3_001332*,
201 *PS3_001331*) showed significantly altered expression in epimutants E5–E6, but these
202 alterations were not associated with sRNA abundance.
203

204 **Heterochromatin marks, along with RNAi, contribute to epigenetic resistance in *M.***
205 ***bainieri***

206 Small RNA spreading has been closely linked to heterochromatin formation and
207 epigenetic gene silencing. Small RNAs targeting specific loci can initiate or reinforce
208 histone modifications, particularly H3K9 methylation [17, 33]. To determine whether
209 histone-mediated epigenetic regulation contributes to FK506 resistance in *M. bainieri*, we
210 conducted chromatin immunoprecipitation (ChIP) to assess the abundance of histone H3
211 lysine 9 dimethylation (H3K9me2) in the following epimutants: E1–E3, which exhibit sRNA
212 spreading; E4, which lacks detectable sRNAs but shows transcriptional repression of *fkbA*
213 and neighboring genes; and E8, a canonical RNAi-dependent, heterochromatin-
214 independent *fkbA* epimutant. ChIP-qPCR was conducted across the *fkbA* locus, targeting
215 the 5′ UTR, two exonic regions, and the 3′ UTR. H3K9me2 enrichment at the positive
216 control region (an siRNA-enriched locus validated by H3K9me2) was comparable across
217 all strains (**Fig 4A**). H3K9me2 levels at the *fkbA* locus were markedly increased in

218 epimutants E1–E4, with fold enrichment ranging from ~5-fold to over 100-fold relative to
219 WT, although the magnitude varied across loci and strains. By contrast, H3K9me2
220 enrichment in E8 and its revertant E8P28 was negligible and comparable to WT. These
221 results indicate that histone modification is associated with unstable antifungal drug
222 resistance in some epimutants (E1-E4) and not others.

223 To further investigate heterochromatin-based epimutational gene silencing, we
224 performed H3K9me2 ChIP-sequencing on the epimutant strains E3, E4, and E8. All
225 strains exhibited similar patterns and levels of H3K9me2 and sRNA at positive control loci,
226 supporting the specificity of the assay (**Fig 4B**). However, in E3 and E4, H3K9me2 signals
227 extended across the *fkbA* locus from neighboring regions, suggesting heterochromatin
228 spreading (**Fig 4C**). Notably, while E3 showed both H3K9me2 and sRNA (distal to *fkbA*),
229 E4 displayed H3K9me2 enrichment without detectable sRNAs. Notably, these ectopic
230 heterochromatic regions spanning *fkbA* were absent in the wild type and revertant isolates.
231 In contrast, the RNAi-dependent epimutant E8 exhibited strong sRNA accumulation
232 specifically at the *fkbA* locus but lacked H3K9me2 enrichment. Taken together, these
233 findings reveal three distinct types of epigenetic strategies underlying FK506 resistance
234 in *M. bainieri* (**Table 3**): RNAi-associated heterochromatin mechanisms (type 1),
235 heterochromatin-dependent only (type 2), and RNAi-dependent only (type 3).
236 Interestingly, type 1 epimutants required fewer passages (average of 6.67) for phenotypic
237 reversion compared to epimutants in type 2 (16.00) or type 3 (18.80), suggesting that
238 dual-layered epigenetic regulation may promote a more readily reversible resistance state.

239 Next, we sought to determine whether gene silencing in these epimutants is
240 regulated at the pre- or post-transcriptional level. Generally, heterochromatin formation

241 compacts chromatin structure, preventing RNA polymerase II (RNAPII) from accessing
242 DNA and thereby blocking transcription initiation, which is classified as pre-transcriptional
243 regulation [34]. In contrast, RNAi pathways typically involve sRNA that target and degrade
244 transcripts after transcription, representing post-transcriptional regulation [35]. To
245 evaluate the transcriptional status of the *fkbA* locus, we performed RNAPII ChIP-qPCR
246 assays. As shown in **Fig 4D**, RNAPII occupancy at a positive control region, *actA*, was
247 comparable across all of the strains, while occupancy at the negative control region,
248 which was enriched for sRNAs and marked by H3K9me2, was negligible in all strains. In
249 contrast, the 5′-UTR, exon, and adjacent regions of *fkbA,* where heterochromatin
250 spreading was observed, was significantly reduced in E3 and E4 compared to WT, the
251 RNAi-dependent epimutant E8, and revertant strains. These findings indicate that gene
252 silencing in type 1 (RNAi-associated heterochromatin mechanisms) and type 2
253 (heterochromatin-dependent only) occurs at the pre-transcriptional level, whereas
254 silencing in type 3 (RNAi-dependent only) operates exclusively through post-
255 transcriptional regulation.
256

257 **Heterochromatin mediates FK506 resistance in *M. atramentarius***

258 In *M. atramentarius*, canonical DNA 5-methylcytosine methyltransferases (DNMT1,
259 DIM-2, RID-1, DNMT4, and DNMT5) were also absent, consistent with a previous study
260 (**S3A Fig**) [29]. Moreover, 5mC analysis in the wild type detected no cytosine methylation,
261 suggesting that DNA methylation is not involved in FK506 resistance (**S3B Fig**). We next
262 assessed whether RNAi- or heterochromatin-based resistance mechanisms identified in
263 *M. bainieri* also operate in *M. atramentarius*, another member of the *Mucor circinelloides*

264 species complex. To evaluate the potential involvement of RNAi, we performed sRNA
265 sequencing of WT, two FK506-resistant epimutants, and their corresponding revertant
266 strains. As shown in **Fig 5A**, antisense sRNA spreading was observed across the *fkbA*
267 locus and its flanking regions. Although sRNA abundance at *fkbA* itself was limited (**S6**
268 and **S7B Fig**), overall the sRNAs exhibited a strong 5′ uridine bias (**S7C Fig**) and a length
269 distribution peaking at 21–24 nt (**S7D Fig**), consistent with canonical RNAi-derived
270 sRNAs. Interestingly, while the spreading pattern resembled that observed in
271 heterochromatin-associated epimutants of *M. bainieri* (**Figs 3A** and **5A**), *M. bainieri*
272 accumulated markedly higher levels of sRNAs at genes flanking the *fkbA* locus compared
273 to *M. atramentarius* (**S4** and **S6 Figs**).

274 To further determine whether the resistant isolates of *M. atramentarius* also involve
275 heterochromatin-associated mechanisms, we next examined histone modification. ChIP-
276 qPCR revealed significant H3K9me2 enrichment at the *fkbA* locus in the epimutants, with
277 fold enrichment ranging from ~12-fold to over 60-fold relative to WT (**Fig 5B**). While
278 H3K9me2 enrichment at the GremLINE1 transposon, used as a positive control, was
279 comparable across all strains, expanded H3K9me2 signals at *fkbA* and its neighboring
280 genes, accompanied by sRNA spreading, were strikingly observed exclusively in the
281 epimutant (**Figs 5C** and **5D**). Consistently, RT-qPCR revealed significantly reduced
282 expression of *fkbA*-neighboring genes in the epimutants compared to WT and revertant
283 strains (**S8 Fig**). Furthermore, consistent with observations in *M. bainieri*, we detected a
284 significant decrease in RNAPII enrichment at the 5′-UTR, exon, and neighboring regions
285 of *fkbA* in the *M. atramentarius* epimutant, indicating that heterochromatin-mediated gene
286 silencing in *M. atramentarius* is associated with pre-transcriptional regulation (**Fig 5E**).

287 Collectively, these results support the conservation of heterochromatin-mediated FK506
288 resistance in *M. atramentarius*, reinforcing its role as a general epigenetic mechanism
289 across the *Mucor circinelloides* complex.
290

291 **Antifungal resistance mediated by heterochromatin is stably inherited following *in***
292 ***vivo* infection**

293 Previous studies reported that RNAi-mediated antifungal resistance can be stably
294 transmitted following *in vivo* passage [36]. To investigate whether heterochromatin-
295 mediated resistance also persists through cell division and stress during host infection,
296 we first examined the maximum growth temperature of *M. bainieri* and *M. atramentarius*
297 with *M. circinelloides* serving as a positive control for growth. *M. atramentarius* was able
298 to grow at 37°C, suggesting potential pathogenicity, whereas *M. bainieri* failed to grow at
299 37°C (**Fig 6A**). This was further confirmed in a murine model, as mice infected with *M.*
300 *atramentarius* exhibited significantly reduced survival, comparable to that observed with
301 *M. circinelloides*, a known pathogen that causes mucormycosis (**Fig 6B**). Notably,
302 infection with *M. atramentarius* also led to a marked decrease in survival, demonstrating
303 its pathogenic potential.

304 Based on these findings, we infected immunosuppressed mice with equal number
305 of spores from WT, FK506-resistant epimutant (E1), and revertant (E1P32) strains of *M.*
306 *atramentarius*. On day 4 post-infection, brain, liver, spleen, and lung tissues were
307 harvested to assess fungal dissemination. Fungal burden was comparable across strains,
308 with no significant differences observed (**S9A Fig**). Subsequently, when fungal colonies
309 recovered from each organ were tested on FK506-containing media, resistance was

310 retained in colonies derived from epimutant-infected mice (over 80% across organs) in
311 contrast to those derived from WT and revertant strains (**Fig 6C**). Interestingly, a few
312 colonies recovered from the lungs of WT- and revertant-infected mice also exhibited
313 FK506 resistance. Sequencing of the *fkbA* locus in FK506-resistant isolates recovered
314 from each organ of WT-, epimutant-, and revertant-infected mice revealed no mutations,
315 with sequences identical to the wild type, indicating that these isolates represent
316 epimutants rather than Mendelian mutants (**S9B Fig** and **S3 Table**). Given that
317 heterochromatin mediates FK506 resistance in epimutants, we next asked whether this
318 epigenetic state persists following *in vivo* infection. To address this, we performed ChIP-
319 qPCR on fungal colonies recovered from four organs. FK506-resistant epimutants
320 exhibited robust H3K9me2 enrichment not only at exonic regions but also across the *fkbA*
321 promoter and terminator (**Fig 6D** and **S10B Fig**). By contrast, H3K9me2 levels were
322 minimal or undetectable in WT and revertant strains. These findings indicate that
323 heterochromatin-mediated antifungal resistance is largely stable during host infection,
324 likely maintained through mitotic inheritance of H3K9 methylation marks.

325 To further examine whether epimutant stability persists over longer periods of
326 infection, we extended our *in vivo* assays by administering a lower dose of
327 cyclophosphamide (an immunosuppressant) or without cyclophosphamide treatment and
328 then assessed FK506 resistance and heterochromatin-associated stability after two or
329 four weeks. Unlike the results observed at 4 days post-infection, fungal burden at 2 weeks
330 post-infection with lower or no cyclophosphamide, and at 4 weeks post-infection without
331 cyclophosphamide, was detected only in the liver and spleen, but not in the brain or lung
332 (**S11A-S11C Figs**). Next, when fungal colonies recovered from the liver and spleen were

333 tested on FK506-containing medium, resistance was retained in colonies derived from
334 epimutant-infected mice at frequencies greater than 50% under all conditions tested (**Figs**
335 **7A, 7C, and 7E**). With resistant colonies from liver and spleen, we sequenced the *fkbA*
336 locus, confirming that there were no mutations, with sequences identical to the wild type
337 (**S11D-S11F Figs** and **S4-S6 Tables**). Furthermore, ChIP-qPCR analysis revealed that
338 FK506-resistant epimutants exhibited H3K9me2 enrichment at the *fkbA* locus (**Figs 7B,**
339 **7D,** and **7F**). Together, these results demonstrate that heterochromatin-mediated
340 antifungal resistance in *M. atramentarius* is stably maintained during prolonged host
341 infection, independent of genetic mutations, and is instead sustained by mitotically
342 inherited H3K9me2 marks.

343 **Discussion**

344 Fungal antimicrobial resistance (fAMR) represents an urgent and growing global
345 health threat, jeopardizing human and animal health, agriculture, and food security [7].
346 Although antifungal drugs are widely used to mitigate this burden, the remarkable
347 adaptability of fungi to chemical stressors has rendered them increasingly difficult to
348 control. Paradoxically, dual antifungal therapies intended to improve treatment outcomes
349 may instead accelerate the evolution of multidrug-resistant strains [37-39]. A deeper
350 understanding of the mechanisms driving fAMR is critical for developing effective
351 interventions across clinical and environmental settings.

352 FK506 targets FKBP12, a conserved protein that when bound to FK506 inhibits
353 the calcineurin pathway—an essential regulator of fungal growth, morphogenesis, stress
354 responses, and virulence [40]. In *M. circinelloides*, FK506 enforces a morphological shift
355 from hyphae to yeast cells, thereby attenuating pathogenicity [28]. Here, we show that
356 FK506 regulates morphology across the *Mucor circinelloides* complex (**S1 Fig**), and that
357 resistance arises via both Mendelian and non-Mendelian mechanisms (**Fig 1** and **Table1**).
358 Our findings expand current models of antifungal resistance by revealing that RNAi- or
359 heterochromatin-mediated epimutations represent alternative, and sometimes
360 independent, pathways. These mechanisms may function separately or synergistically to
361 silence *fkbA*, operating through either post-transcriptional or pre-transcriptional regulation
362 to confer FK506 resistance, and resulting in resistance phenotypes with varying degrees
363 of stability, specificity, and reversibility (**Fig 8**).

364 In nature, diverse microorganisms, including bacteria, viruses, and fungi, interact
365 continuously, forming complex ecological networks [41-44]. Soil systems are nutrient-rich

366 environments that support a vast diversity of microorganisms, which in turn contribute to
367 essential ecological functions such as nutrient cycling and organic matter decomposition
368 [45, 46]. *Streptomyces* is one of the most widely distributed and ecologically significant
369 genera within the phylum Actinobacteria, renowned for its remarkable ability to produce
370 a wide variety of bioactive secondary metabolites, including antifungal compounds[47].
371 Here, we studied FK506, a natural antifungal compound that is produced by several
372 *Streptomyces* species, such as *Streptomyces hygroscopicus* and *Streptomyces*
373 *tsukubaensis* [48, 49]. Mucorales represent a major fungal order of soil-dwelling
374 saprophytic fungi [50], and thus the ecological coexistence of *Streptomyces* and *Mucor*
375 in soil raises the possibility that natural occurrence of the antifungal natural product FK506
376 may impose a selective pressure on fungal populations. This pressure may promote the
377 emergence of epigenetic resistance, even in the absence of anthropogenic drug use, by
378 enabling fungi to flexibly modulate gene expression in response to environmental
379 antifungal stress. Interestingly, amphotericin B, the primary first-line therapy for
380 mucormycosis, is also a natural product produced by *Streptomyces nodosus* [51]. This
381 raises the possibility that fungi may encounter antifungal pressures in nature, allowing
382 epigenetic resistance mechanisms to evolve as strategies that enhance survival and
383 competitive fitness in chemically dynamic ecosystems.

384 Our data revealed that the size distribution of sRNAs at the *fkbA* locus differs from
385 those mapped to neighboring genes (**Fig 3, S5** and **S7 Figs**). The predominant sRNAs
386 derived from *fkbA* were 21 and 24 nt, whereas most neighboring genes displayed stronger
387 accumulation at 23–24 nt. Previous work in *Mucor* proposed that different sRNA size
388 classes may serve distinct roles in silencing, with 21-nt sRNAs acting as the predominant

389 species involved in target mRNA degradation [52]. In this context, the increased
390 abundance of 21 nt sRNAs derived specifically from *fkbA* suggests that FK506-resistant
391 epimutants may preferentially generate the sRNA class most directly linked to efficient
392 target degradation. A similar phenomenon was also reported at the *pyrG* and *pyrF* loci,
393 where sRNAs fell within the 21–24 nt range but showed locus differences. *pyrG* sRNAs
394 were enriched at 21 and 24 nt, whereas *pyrF* sRNAs were predominantly 23–24 nt [16].
395 Such variation may result from multiple, non-mutually exclusive mechanisms. First,
396 differential usage of Dicer paralogs may contribute. In *M. circinelloides*, DCL2 produces
397 23–24 nt siRNAs, whereas DCL1 can result in more heterogeneous size distributions
398 including 21 nt [53, 54]. Similarly, in the model plant *Arabidopsis thaliana*, DCL4 primarily
399 generates 21-nt siRNAs, while DCL3 is responsible for 24-nt siRNAs involved in
400 transcriptional silencing [55, 56]. Second, substrate properties of the transcripts, including
401 secondary structure, GC content, and overall architecture, may influence Dicer
402 processing efficiency and cleavage-site preference, thereby generating distinct size
403 profiles [57, 58]. These observations suggest that even within the canonical RNAi
404 framework, locus-specific features may shape distinct sRNA size distributions.

405 The interplay between RNAi and histone methylation raises key questions about
406 the sequence and causality of these silencing events. Preexisting heterochromatin can
407 initiate RNAi, as seen in centromeres and transposable elements in *S. pombe* and
408 *Arabidopsis thaliana*, where transcripts from heterochromatic loci are processed into
409 siRNAs that reinforce silencing [59]. In *S. pombe*, small RNAs bound to Argonaute form
410 the RNA-induced transcriptional silencing (RITS) complex with the chromodomain protein
411 Chp1 and the bridging protein Tas3. Chaperone proteins such as Hsp90 stabilize RITS

412 complex, which recruits Clr4 to nascent transcripts, thereby facilitating heterochromatin
413 formation [59, 60]. Stc1 associates with Ago1 and recruits the chromatin-modifying CLRC
414 complex (Clr4-Rik1-Cul4-Dos1-Dos2), underscoring its critical role in connecting RNAi
415 with heterochromatin formation [61]. Meanwhile, euchromatic loci may sporadically
416 generate double-stranded RNA, initiating RNAi and leading to heterochromatin deposition
417 via a positive feedback loop involving the RITS complex and Clr4 [62]. [62]. Interestingly,
418 in our study, we identified FK506-resistant epimutants with varying combinations of siRNA
419 accumulation and H3K9me2 enrichment at the *fkbA* locus (**Fig 4**). These findings support
420 several non-exclusive models: (1) RNAi-driven initiation of heterochromatin, (2)
421 heterochromatin-facilitated RNAi, or (3) other mechanisms.

422 To explore the first hypothesis, we conducted a comparative analysis of RNAi,
423 H3K9 methylation-based heterochromatin formation, and RITS components across *M.*
424 *bainieri*, *M. atramentarius*, *M. lusitanicus*, and *M. circinelloides* to assess the potential
425 coupling between RNAi and heterochromatin pathway. As reported previously in *M.*
426 *lusitanicus* [30], the RITS components Chp1 and Tas3 are absent across all four *Mucor*
427 species, whereas the bridging protein Stc1, the histone methyltransferase Clr4, and
428 CLRC complex subunits (Rik1, Cul4, and Raf1) are conserved (**S12 Fig**). Thus, although
429 elements of the coupling machinery such as Stc1 and CLRC are conserved, the apparent
430 absence of a complete RITS complex suggests that the connection between RNAi and
431 heterochromatin may operate in a partial or context-dependent manner. Under FK506
432 selective pressure, RNAi may be initiated at the *fkbA* locus, leading in some cases to the
433 establishment of heterochromatin, while in others, RNAi may act independently. Even

434 when heterochromatin is formed, weak or transient interactions between RNAi and
435 heterochromatin could result in heterochromatin-only epimutants.

436 Second, preexisting heterochromatin could facilitate RNAi, serving as a template
437 for small RNA generation. To explore this possibility, we analyzed the distribution of H3K9
438 dimethylation and sRNA in wild-type strains of four *Mucor* species (*M. bainieri*, *M.*
439 *atramentarius*, *M. lusitanicus*, and *M. circinelloides*). As shown in **S13 Fig**, discrete
440 H3K9me2 islands were detected downstream of *fkbA* in all four species, suggesting that
441 preexisting heterochromatin on transposon-rich regions may spread toward the *fkbA*
442 locus under FK506 selective pressure and recruit the RNAi machinery to generate small
443 RNAs. Similar phenomena have been reported in other organisms. In *S. pombe*, for
444 example, caffeine stress triggers redistribution of H3K9 methylation and evokes sRNA
445 generation [17]. Interestingly, these H3K9me2 islands lacked detectable sRNAs in *M.*
446 *lusitanicus* and *M. circinelloides*, whereas the co-occurrence of H3K9me2 and sRNAs
447 was observed in *M. bainieri* and *M. atramentarius*, raising the possibility that the
448 relationship between RNAi and heterochromatin formation may interact differently across
449 species.

450 Third, RNAi and heterochromatin formation may occur simultaneously under
451 FK506 pressure but act independently without functional coupling. A previous study
452 reported that RNAi and heterochromatin formation can function independently to repress
453 GremLINE1 transposable elements and maintain genome stability in *M. lusitanicus* [30].
454 Thus, it is possible that, upon FK506 exposure, these machineries were independently
455 activated at the same genomic region, with RNAi generating sRNAs at the *fkbA* locus and
456 heterochromatin spreading from adjacent transposon-rich regions, resulting in their

457 apparent coexistence without direct mechanistic interaction. Taken together, future
458 studies analyzing pathway-specific mutants will be critical to determine the directionality
459 and mechanistic coupling or uncoupling of these epigenetic processes.

460 Beyond FK506-induced dynamics at the *fkbA* locus, our comparative genomic
461 analyses across four *Mucor* species provide additional insight into how RNAi and
462 heterochromatin interplay may differ among species. GremLINE elements are present in
463 *M. atramentarius*, *M. lusitanicus*, and *M. circinelloides*, where they reside within or near
464 putative centromeric regions, but are absent from the *M. bainieri* genome (**S14 Fig**). The
465 centromeric GremLINEs in these species consistently show strong H3K9me2 enrichment,
466 supporting their association with heterochromatic domains. Notably, *M. bainieri* exhibits
467 a distinct architecture. Although it lacks GremLINEs, its putative centromeric regions are
468 enriched for a different repeat, TE00000158, which is associated with strong H3K9me2.
469 This pattern diverges sharply from the GremLINE-associated uncoupling observed in *M.*
470 *circinelloides*, raising the possibility that *M. bainieri* may have evolved a species-specific
471 centromeric repeat landscape and RNAi-heterochromatin relationship. Collectively, these
472 comparative observations suggest that the interplay between RNAi and heterochromatin
473 may not be conserved and may vary across species, likely influenced by species-specific
474 differences in repeat landscapes and centromere architecture.

475 Torres-Garcia et al. demonstrated that external stressors such as caffeine induce
476 phenotypic plasticity via Clr4/H3K9me "read-write" systems in *S. pombe*, underscoring
477 the adaptive function of heterochromatin in non-pathogenic yeast [17]. Our findings
478 extend this concept by providing direct evidence that H3K9 methylation contributes to
479 FK506 resistance in dimorphic *Mucor* species. Notably, this mechanism operates in the

480 non-pathogenic species *M. bainieri* and *M. atramentarius* species, a species with
481 pathogenic potential, suggesting that heterochromatin-mediated resistance is conserved
482 across diverse fungal taxa, spanning both unicellular yeasts and multinuclear hyphal
483 species. While RNAi-dependent antifungal resistance has been shown to be rapidly
484 induced and reversed following *in vivo* passage in a murine model [36], the *in vivo* stability
485 of heterochromatin-dependent epimutants has not been previously characterized. Here,
486 we demonstrate that a heterochromatin-dependent epimutant remains stable *in vivo* (**Fig**
487 **6** and **Fig 7**). The persistence, even in the absence of antifungal pressure, raises the
488 possibility that epigenetically resistant strains could silently disseminate in clinical settings,
489 complicating diagnostics and treatment.

490 In summary, our study extends RNAi-dependent gene silencing to additional
491 *Mucor* species and uncovers that heterochromatin-mediated silencing also drives
492 antifungal resistance. These findings underscore the remarkable epigenetic plasticity of
493 fungal epigenomes and highlight adaptive strategies that enable reversible, yet durable,
494 resistance. Targeting RNAi and chromatin-modifying pathways may thus represent a
495 promising therapeutic strategy against fAMR.

496 **Material and methods**

497 **Fungal strains, media and growth conditions**

498 *Mucor* strains studied here are described in **S1 Table**. *Mucor* strains were grown
499 on liquid or solid yeast extract peptone dextrose (YPD; BD, Difco, Franklin Lakes, NJ,
500 USA) at room temperature. To isolate FK506-/rapamycin-resistant strains, 10^5 spores
501 were inoculated onto more than ten solid YPD, supplemented with antifungal drug 1
502 μg/mL of FK506 (Astellas Pharma, Chuo, Tokyo, Japan) and 100 ng/ml of rapamycin (API
503 Chem, Hangzhou, Zhejiang, Chian) and incubated for 3, 5, 7 days [15]. To test the stability
504 of FK506-resistant strains, spores of the resistant strains were collected and inoculated
505 in liquid YPD without any drugs overnight [16]. These were then serially subcultured
506 overnight for several rounds, after which the passaged cells were spotted onto YPD or
507 YPD supplemented with FK506 to confirm phenotypic plasticity.

508

509 **Illumina sequencing and genome assembly**

510 *Mucor* mycelium were grown on YPD medium, harvested, frozen in liquid nitrogen,
511 and ground into a find powder. Genomic DNA samples were prepared using Norgen
512 Biotek Yeast/Fungi Genomic DNA Isolation Kit (Ontario, Canada). Genomic DNA libraries
513 were constructed with Roche KAPA HyperPrep Kit. 150-bp paired-end reads were
514 obtained utilizing the NovaSeq X Plus sequencing system (Illumina) at the Duke
515 Sequencing and Genomic Technologies Core (SGT). Raw reads were checked for quality
516 metrics using FastQC v0.11.7 and processed by fastp v0.23.4 to remove adapters and
517 low-quality bases or reads. Genomes were assembled using SPAdes v3.15.5 set to

518 isolate default mode. Genome assemblies were cleaned, sorted, masked, and annotated
519 using the Funannotate v1.8.15 [63].
520
521 **Nanopore sequencing and genome assembly**
522 A total of 10^6 spores from *M. bainieri* and *M. atramentarius* wild-type strains were
523 inoculated into liquid YPD medium and incubated overnight at 25 °C. Cells were
524 harvested by centrifugation, washed with distilled water, frozen with liquid nitrogen, and
525 ground with a mortar and pestle. High-molecular-weight (HMW) DNA was extracted from
526 each sample using the Monarch HMW DNA Extraction Kit for Tissue (NEB, Ipswich, MA,
527 USA) according to the manufacturer's protocol. DNA concentration and quality were
528 assessed using a NanoDrop spectrophotometer (ThermoFisher, Waltham, MA, USA) and
529 a Qubit fluorometer with the Qubit dsDNA High Sensitivity kit (ThermoFisher). DNA
530 integrity was confirmed by CHEF electrophoresis performed at 6.0 V in a 1% agarose gel
531 for 18 hours, which revealed intact HMW DNA. Libraries were prepared using the ligation
532 sequencing kit V14 (SQK-LSK114; Oxford Nanopore Technologies, Oxford, United
533 Kingdom) and sequenced on MinION R10.4.1 flow cells (ONT; Oxford Nanopore
534 Technologies) following to the manufacturer's protocol in-house in our laboratory.
535 POD5 base calling was performed with the Dorado basecaller (v0.5.2; Oxford
536 Nanopore Technologies, https://github.com/nanoporetech/dorado). Demultiplexing and
537 BAM-to-FASTQ conversion were carried out using Dorado demux (v0.5.2). The resulting
538 FASTQ files were error-corrected with Canu (v2.2) and assembled using Flye (v2.9.5-
539 b1801) [64, 65]. The expected genome size was set to 50 Mb, and a minimum overlap
540 length of 5 kb was required between reads. The assembled genome was subsequently

541 polished in three iterations using Pilon (v1.24; Broad Institute,
542 https://github.com/broadinstitute/pilon/releases/tag/v1.24) with default parameters
543 utilizing the raw Illumina sequencing data deposited under NCBI BioProject accessions
544 PRJNA1277536 (*M. bainieri* CBS293.63) and PRJNA1277544 (*M. atramentarius*
545 CBS202.28). Repetitive sequences were identified using RepeatMasker (v4.1.5;
546 https://www.repeatmasker.org) with default parameters and genome annotation was
547 performed using Funannotate (v1.8.17) with the masked genome assembly and strain-
548 specific RNA-seq alignments [63]. This pipeline produced high-quality genome
549 assemblies, with *M. bainieri* assembled into 30 contigs (N50 = 6 Mb; 98.7% BUSCO
550 completeness; 9,781 predicted genes) and *M. atramentarius* into 33 contigs (N50 = 2 Mb;
551 98.8% BUSCO completeness; 11,597 predicted genes).
552
553 **The *fkbA* and calcineurin gene sequencing analysis**
554 *Mucor* strains were cultured on YPD medium for three days. Approximately 1–5
555 mg of harvested cells was suspended in 300 μL Tissue & Cell Lysis Buffer (Lucigen,
556 Middleton, WI, USA) and 1 μL proteinase K (ThermoFisher). The mixture was incubated
557 at 65°C for 45 min, followed by the addition of 150 μL MPC Protein Precipitation Reagent
558 (Lucigen). After centrifugation, the pellet was washed with 70% ethanol and resuspended
559 in distilled water, and genomic DNA (gDNA) quality was analyzed using a Qubit and a
560 NanoDrop (ThermoFisher). The promoter, open reading frame, and terminator regions of
561 the *fkbA* gene were amplified by polymerase chain reaction (PCR) using primers listed in
562 **S2 Table**. The purified PCR products were sequenced using long read sequencing with

563 ONT at Plasmidsaurus Inc. (Eugene, CA, USA) and analyzed against the reference *fkbA*
564 sequence using Clustal Omega (v1.2.3).
565
566 **RNA extraction and quantitative PCR (qPCR) analysis**
567 Total RNA was extracted from 10 mg of *Mucor* cells cultured on YPD, with or
568 without FK506, at room temperature. After overnight lyophilization, each sample was
569 homogenized in a FastPrep bead-beater (MP Biomedicals, Santa Ana, CA, USA) with 0.2
570 mL of zirconia-silica beads (BioSpec Products, Bartlesville, OK, USA). Total RNA was
571 then purified with the miRNeasy Mini Kit (Qiagen, Hilden, Germany) and RNA quantity
572 and quality were analyzed using a Nanodrop (Thermo Fisher) and a Qubit Fluorometer
573 with Qubit RNA High Sensitivity kit (ThermoFisher) [66]. The isolated RNA was treated
574 with DNase and subsequently employed for cDNA synthesis with the Maxima H Minus
575 cDNA Synthesis Master Mix (ThermoFisher, Waltham, MA, USA). Real-time PCR was
576 performed with PowerUp SYBR Green Master Mix (ThermoFisher) on a QuantStudio 3
577 qPCR system (ThermoFisher) in technical triplicate. The primers for qPCR are listed in
578 **S2 Table**. Gene expression was normalized to *actA*, relative fold expression was
579 calculated using $2^{-\Delta\Delta Ct}$ method.
580
581 **Small RNA (sRNA) sequencing**
582 sRNA libraries were constructed with the QIAseq miRNA Library Kit (Qiagen) and
583 sequenced on an NovaSeq X platform (Illumina) by 75-bp single end. Raw reads were
584 trimmed with adaptor sequence (5′-GTTCAGAGTTCTACAGTCCGACGATC-3′ and 5′-
585 AACTGTAGGCACCATCAA-3′) utilizing BBDuk. Filtered reads were then mapped to the

586 reference genomes (*M. bainieri* CBS293.63; PRJNA1277536 or *M. atramentarius*
587 CBS202.28; PRJNA1277544) using BBMap with default parameters (last modified
588 September 15, 2022) [67]. The resulting SAM files were converted to BAM files, and
589 antisense reads were sorted using SAMtools (v1.21) [68]. BAM files were converted to
590 TDF files using IGV tools with a window size of 20 bp and the mean window function. The
591 data was subsequently visualized in the Integrative Genome Viewer (IGV v2.16.0), where
592 the Y-axis represents the average read coverage per 20-bp window [69]. The Y-axis
593 reflects the average read coverage per 20 bp window. Peak calling was performed with
594 MACS3 using the --nomodel option with an extension size of 147 bp. sRNA-seq
595 experiments were performed with one biological sample per strain.
596
597 **Western blot**
598 Each *Mucor* strain was cultivated in YPD, with or without FK506, at room
599 temperature for three days. Ten milligrams of *Mucor* cells were lyophilized overnight and
600 homogenized using a FastPrep bead-beater (MP Biomedicals) with 0.2 mL of zirconia-
601 silica beads (BioSpec Products). Pierce RIPA buffer (ThermoFisher) containing a
602 protease inhibitor tablet (Roche) was then added, and each sample was further disrupted
603 with a FastPrep bead-beater. The samples were incubated on ice for at least 30 min. Cell
604 extracts were centrifuged at 14,000 RPM, 4°C for 10 min, and the supernatants were
605 quantified with the Pierce BCA Protein Assay Kit (ThermoFisher). Next, 20 µg of each
606 sample was mixed with Novex Tris-Glycine SDS Sample Buffer (Invitrogen, Waltham, MA,
607 USA) and boiled at 85°C for 5 min. After briefly cooling, the samples were separated by
608 SDS-PAGE, transferred to a PVDF membrane, and incubated overnight at 4°C with an

609 anti-FKBP12 antibody (Invitrogen) or an anti-GAPDH antibody (Proteintech, Rosemont,
610 IL, USA). Following incubation with a horseradish peroxidase-conjugated anti-rabbit
611 antibody, FKBP12 and GAPDH expression were detected on a ChemiDoc MP imaging
612 system (Bio-Rad, Hercules, CA, USA).
613
614 **Chromatin immunoprecipitation (ChIP)-qPCR**
615 A total of 10^6 spores from each *Mucor* strain were inoculated in liquid YPD medium
616 with or without FK506 and incubated overnight at 25°C. The samples were then cross-
617 linked with 1% formaldehyde (ThermoFisher), followed by addition of glycine (Sigma-
618 Aldrich, St. Louis, MO, USA) at a final concentration of 0.125M. After washing and
619 freezing using liquid nitrogen, each sample was ground with a pestle and suspended in
620 ChIP lysis buffer (50 mM HEPES, pH=7.5, 150 mM NaCl, 1 mM EDTA, pH=8, 1% Triton
621 X-100, and 0.1% sodium deoxycholate) containing a protease inhibitor tablet (Roche).
622 Disrupted cells were then sonicated with a Bioruptor (Diagenode) for 40 cycles, with 30s
623 on and 30s off and clarified by centrifuge for 5 min. The input samples were stored at
624 -80°C, while the IP samples were incubated overnight at 4°C with Dynabeads Protein A/G
625 (Invitrogen) pre-conjugated with the anti-histone H3K9 dimethyl antibody (Abcam,
626 Cambridge, UK) or the anti-RNA polymerase II antibody (Active Motif, Carlsbad, CA).
627 Crosslinking between protein and DNA in both input and IP samples was reversed with
628 the MAGnify Chromatin Immunoprecipitation System (Invitrogen), and DNA quality and
629 quality were assessed using a Nanodrop (Thermo Fisher) and a Qubit Fluorometer with
630 Qubit dsDNA High Sensitivity kit (ThermoFisher). qPCR was performed in technical
631 triplicate with primers described in **S2 Table**. For H3K9me2 ChIP-qPCR, GremLINE1

632 transposon elements were used as positive controls in *M. atramentarius* [30]. However,
633 our analysis of the *M. bainieri* genome suggests the GremLINE1 elements are absent in
634 the Illumina-based genome assembly. Instead, to develop a positive control for the
635 H3K9me2 ChIP-qPCR analysis in *M. bainieri*, we hypothesized that the loci enriched for
636 H3K9m2 should at least partially overlap with the genomic regions enriched for small
637 RNAs. Specifically, we first identified three genomic loci enriched for small RNAs based
638 on our sRNA analysis and then designed primers targeting these loci and tested them for
639 the presence of H3K9me2 signals using ChIP-qPCR. One of the three loc, *PS3_010814*
640 (identified in Illumina-based genome assembly deposited under NCBI SRA
641 PRJNA1277536), exhibited consistent H3K9me2 enrichment across samples including
642 WT, epimutants, and revertants, and was selected as the positive control for the
643 subsequent H3K9me2 ChIP-qPCR analyses. The *actA* gene, which lacks both small RNA
644 accumulation and heterochromatin marks, was used as a negative control. H3K9
645 methylation enrichment was calculated by normalizing the IP DNA to the input DNA with
646 the ΔCt method and further adjusted to the *actA* gene with the ΔΔCt method, followed by
647 $2^{-\Delta\Delta Ct}$ to determine relative enrichment [70, 71]. For RNA polymerase II ChIP-qPCR, the
648 *actA* gene was used as a positive control, as it is transcriptionally active. As a negative
649 control, we selected an intergenic locus defined as an siRNA-producing region embedded
650 within transposable element–rich sequences and associated with H3K9me2
651 heterochromatin. RNA polymerase II enrichment was similarly calculated by using the
652 $2^{-\Delta\Delta Ct}$ method with a negative control, an intronic region enriched for siRNAs and by
653 H3K9me2.

654 **ChIP sequencing**

655 Input and IP libraries were constructed with KAPA HyperPrep (Roche) and
656 sequenced on a NovaSeq X platform (Illumina) by 150-bp paired end. Raw FASTA files
657 were trimmed with Trimmomatic (v0.39) and filtered reads were mapped to the reference
658 genomes (*M. bainieri* CBS293.63; PRJNA1277536 or *M. atramentarius* CBS202.28;
659 PRJNA1277544) using Bowtie2 (v2.5.4) with default parameters [72, 73]. The resulting
660 SAM files were converted to BAM files using SAMtools (v1.21) [68]. Broad ChIP-peak
661 calling was analyzed with MACS3 (v3.0.3) with the parameters --mfold 10 1000 and --
662 extsize 147, and enrichment was analyzed by generating coverage files with
663 BamCoverage (v3.5.6), followed by counts per million (CPM) normalization [74, 75].
664 Processed BAM files were converted to TDF files IGV tools with a window size of 20 bp
665 and the mean window function and subsequently visualized with IGV (v2.16.0) [76]. ChIP-
666 seq experiments were performed with one biological sample per strain.

667

668 ***In vivo* infection**

669 Six-week-old male BALB/cAnNCrl mice, 6 to 7 weeks old obtained from Jackson
670 Laboratory (Bar Harbor, Maine, USA), were analyzed in this study. Five mice were
671 infected with each *Mucor* strain. Two days prior to infection, 200 mg/kg of
672 cyclophosphamide (Sigma-Aldrich), an immunosuppressant, was administered
673 intraperitoneally. Each mouse was infected with 1×10^6 spores (in 50 μL PBS) via retro-
674 orbital injection after anesthetizing the mice with isoflurane for 2.5 min. After infection, the
675 mice were monitored twice daily and administered cyclophosphamide at 200 mg/kg body
676 weight every four days. To assess pathogenicity, weight loss was monitored, and any
677 animal experiencing ≥ 20% loss of body weight was humanely euthanized. To examine

678 epimutant stability, five mice per each strain were subjected under four treatment
679 conditions: (i) cyclophosphamide at 200 mg/kg every 4 days, (ii) cyclophosphamide at 50
680 mg/kg every 4 days for 2 weeks, (iii) no cyclophosphamide for 2 weeks, (iv) no
681 cyclophosphamide treatment for 4 weeks. At the designated time points, mice were
682 sacrificed, and fungal burden and epimutant stability were evaluated. All animal
683 experiments in this study were approved by the Duke University Institutional Animal Care
684 and Use Committee (IACUC) (protocol #A224-23-11). Animal care and experiments were
685 conducted according to IACUC ethical guidelines.
686
687 **Stability of epimutants during *in vivo* infection**
688 To assess fungal burden and isolate *Mucor* strains from organs, five mice per
689 *Mucor* strain were intravenously infected. At the humane endpoint, the brain, lung, liver,
690 and spleen were dissected. Whole organs were homogenized in 0.8 mL of PBS with a
691 bead beater for 2 min, then diluted and plated on YPD supplemented with 50 µg/mL
692 chloramphenicol. After a two-day incubation at room temperature, fungal colonies were
693 picked and patched onto YPD plates with or without FK506 to assess the stability of
694 FK506 resistance following *in vivo* passage. The stability rate was determined by
695 calculating the proportion of resistant colonies on YPD supplemented with FK506 relative
696 to the total colonies patched on YPD [36]. To determine whether resistant isolates were
697 epimutants, genomic DNA was extracted from all resistant isolates, and the *fkbA* region
698 was PCR-amplified and sequenced using long read sequencing with ONT in
699 Plasmidsaurus Inc. (Eugene, CA, USA). In addition, to determine whether the resistant
700 isolates represented heterochromatin-associated epimutants, several resistant isolates
701 were analyzed by ChIP-qPCR.
702

703 **Quantification and statistical analyses**

704 Statistical differences between the control and target strains were evaluated using
705 ordinary one-way ANOVA using Tukey's Honestly Significant Difference (HSD) test with
706 using GraphPad Prism (v10.1.1). Kaplan-Meier survival curves were generated and
707 analyzed with the log-rank test in R (v4.3.2) to estimate survival probability. Data are
708 reported as mean ± standard deviation. In all graphs, p values or asterisks were listed
709 indicating statistical significance ($^{*}p < 0.05$; $^{**}p < 0.01$; $^{***}p < 0.001$; $^{****}p < 0.0001$).

Funding Statement

This study was supported by the NIH/National Institute of Allergy and Infectious Diseases (R01-AI170543-04, R01-AI039115-28, and R01-AI050113-20) awarded to J.H.. J.H. is co-director and fellow of the CIFAR program Fungal Kingdom: Threats & Opportunities.

Acknowledgments

We thank Dr. Vikas Yadav for his insightful advice on bioinformatics analyses as well as for his scientific discussions and critical reading. We are grateful to Dr. María Isabel Navarro-Mendoza for providing guidance on *in vivo* training. We also thank Anna Floyd Averette for her invaluable support and assistance with *in vivo* assays; Ziyan Xu for preparing DNA for Illumina whole genome sequencing; Dr. Jason E. Stajich (University of California) for providing whole-genome sequence datasets and initial preliminary analysis; and Dr. Grit Walther (Hans Knöll Institute) for providing *Mucor* isolates. We appreciate critical reading by Dr. Sheng Sun and Dr. Jun Huang. We thank Devi Swain, Director of the Duke Sequencing and Genomic Technologies Core for technical support.

Author Contributions

Conceptualization: Ye-Eun Son, Joseph Heitman

Methodology: Ye-Eun Son, Carlos Pérez-Arques

Software: Ye-Eun Son, Carlos Pérez-Arques

Validation: Ye-Eun Son

Investigation: Ye-Eun Son, Carlos Pérez-Arques

733 **Visualization**: Ye-Eun Son, Carlos Pérez-Arques

734 **Resources**: Joseph Heitman

735 **Writing – Original Draft**: Ye-Eun Son

736 **Writing – Review & Editing**: Ye-Eun Son, Carlos Pérez-Arques, Joseph Heitman

737 **Supervision**: Joseph Heitman

738 **Funding Acquisition**: Joseph Heitman

739

740 **Competing interests**

741 The authors declare no conflicts of interest.

742

743 **Data Availability**

744 Small RNA-seq, ChIP-seq, Nanopore sequencing data, and the corresponding
745 genome assemblies are available in the NCBI SRA under project accession numbers
746 PRJNA1242486 (*M. bainieri* CBS293.63) and PRJNA1242487 (*M. atramentarius*
747 CBS202.28). Illumina whole-genome sequencing data are available under project
748 accession numbers PRJNA1277536 (*M. bainieri* CBS293.63) and PRJNA1277544 (*M.*
749 *atramentarius* CBS202.28).

750 **References**

751 1. Case NT, Gurr SJ, Fisher MC, Blehert DS, Boone C, Casadevall A, et al. Fungal
752 impacts on earth's ecosystems. Nature. 2025;638(8049):49-57. pmid: 39910383.
753 2. McDermott A. Drug-resistant fungi on the rise. Proc Natl Acad Sci U S A.
754 2022;119(48):e2217948119. pmid: 36413501.
755 3. Fisher MC, Denning DW. The WHO fungal priority pathogens list as a game-
756 changer. Nat Rev Microbiol. 2023;21(4):211-2. pmid: 36747091.
757 4. Lockhart SR, Chowdhary A, Gold JAW. The rapid emergence of antifungal-
758 resistant human-pathogenic fungi. Nat Rev Microbiol. 2023;21(12):818-32. pmid:
759 37648790.
760 5. Perlin DS, Rautemaa-Richardson R, Alastruey-Izquierdo A. The global problem
761 of antifungal resistance: prevalence, mechanisms, and management. Lancet
762 Infect Dis. 2017;17(12):e383-e92. pmid: 28774698.
763 6. Nnadi NE, Carter DA. Climate change and the emergence of fungal pathogens.
764 PLoS Pathog. 2021;17(4):e1009503. pmid: 33914854.
765 7. Fisher MC, Burnett F, Chandler C, Gow NAR, Gurr S, Hart A, et al. A one health
766 roadmap towards understanding and mitigating emerging fungal antimicrobial
767 resistance: fAMR. NPJ Antimicrob Resist. 2024;2(1):36. pmid: 39524479.
768 8. Lee Y, Robbins N, Cowen LE. Molecular mechanisms governing antifungal drug
769 resistance. NPJ Antimicrob Resist. 2023;1(1):5. pmid: 38686214.
770 9. Al Aboud NM, Tupper C, Jialal I. Genetics, epigenetic mechanism. StatPearls.
771 Treasure Island (FL)2025.
772 10. Flowers SA, Colon B, Whaley SG, Schuler MA, Rogers PD. Contribution of
773 clinically derived mutations in *ERG11* to azole resistance in *Candida albicans*.
774 Antimicrob Agents Chemother. 2015;59(1):450-60. pmid: 25385095.
775 11. Lewis RE, Liao G, Hou J, Prince RA, Kontoyiannis DP. Comparative *in vivo*
776 dose-dependent activity of caspofungin and anidulafungin against echinocandin-
777 susceptible and -resistant *Aspergillus fumigatus*. J Antimicrob Chemother.
778 2011;66(6):1324-31. pmid: 21486855.
779 12. Nagy G, Kiss S, Varghese R, Bauer K, Szebenyi C, Kocsube S, et al.
780 Characterization of three pleiotropic drug resistance transporter genes and their
781 participation in the azole resistance of *Mucor circinelloides*. Front Cell Infect
782 Microbiol. 2021;11:660347. pmid: 33937100.
783 13. Navarro-Mendoza MI, Perez-Arques C, Parker J, Xu Z, Kelly S, Heitman J.
784 Alternative ergosterol biosynthetic pathways confer antifungal drug resistance in
785 the human pathogens within the *Mucor* species complex. mBio.
786 2024;15(8):e0166124. pmid: 38980037.
787 14. Chang Z, Yadav V, Lee SC, Heitman J. Epigenetic mechanisms of drug
788 resistance in fungi. Fungal Genet Biol. 2019;132:103253. pmid: 31325489.
789 15. Calo S, Shertz-Wall C, Lee SC, Bastidas RJ, Nicolas FE, Granek JA, et al.
790 Antifungal drug resistance evoked via RNAi-dependent epimutations. Nature.
791 2014;513(7519):555-8. pmid: 25079329.
792 16. Chang Z, Billmyre RB, Lee SC, Heitman J. Broad antifungal resistance mediated
793 by RNAi-dependent epimutation in the basal human fungal pathogen *Mucor*
794 *circinelloides*. PLoS Genet. 2019;15(2):e1007957. pmid: 30742617.

795 17. Torres-Garcia S, Yaseen I, Shukla M, Audergon P, White SA, Pidoux AL, et al.
796 Epigenetic gene silencing by heterochromatin primes fungal resistance. Nature.
797 2020;585(7825):453-8. pmid: 32908306.
798 18. Hernández JL, Buckley CJ. Mucormycosis. StatPearls. Treasure Island
799 (FL)2025.
800 19. Binder U, Maurer E, Lass-Florl C. Mucormycosis--from the pathogens to the
801 disease. Clin Microbiol Infect. 2014;20 Suppl 6:60-6. pmid: 24476149.
802 20. Lax C, Nicolas FE, Navarro E, Garre V. Molecular mechanisms that govern
803 infection and antifungal resistance in Mucorales. Microbiol Mol Biol Rev.
804 2024;88(1):e0018822. pmid: 38445820.
805 21. Cornely OA, Alastruey-Izquierdo A, Arenz D, Chen SCA, Dannaoui E,
806 Hochhegger B, et al. Global guideline for the diagnosis and management of
807 mucormycosis: an initiative of the european onfederation of medical mycology in
808 cooperation with the mycoses study group education and research consortium.
809 Lancet Infect Dis. 2019;19(12):e405-e21. pmid: 31699664.
810 22. Roden MM, Zaoutis TE, Buchanan WL, Knudsen TA, Sarkisova TA, Schaufele
811 RL, et al. Epidemiology and outcome of zygomycosis: a review of 929 reported
812 cases. Clin Infect Dis. 2005;41(5):634-53. pmid: 16080086.
813 23. Devnath P, Dhama K, Tareq AM, Emran TB. Mucormycosis coinfection in the
814 context of global COVID-19 outbreak: A fatal addition to the pandemic spectrum.
815 Int J Surg. 2021;92:106031. pmid: 34311126.
816 24. WHO. WHO fungal priority pathogens list to guide research, development and
817 public health action2022.
818 25. Wagner L, Stielow JB, de Hoog GS, Bensch K, Schwartze VU, Voigt K, et al. A
819 new species concept for the clinically relevant *Mucor circinelloides* complex.
820 Persoonia. 2020;44:67-97. pmid: 33116336.
821 26. Perez-Arques C, Navarro-Mendoza MI, Xu Z, Walther G, Heitman J. RNAi
822 epimutations conferring antifungal drug resistance are inheritable. Nat Commun.
823 2025;16(1):7293. pmid: 40775213.
824 27. Lee SC, Li A, Calo S, Inoue M, Tonthat NK, Bain JM, et al. Calcineurin
825 orchestrates dimorphic transitions, antifungal drug responses and host-pathogen
826 interactions of the pathogenic mucoralean fungus *Mucor circinelloides*. Mol
827 Microbiol. 2015;97(5):844-65. pmid: 26010100.
828 28. Lee SC, Li A, Calo S, Heitman J. Calcineurin plays key roles in the dimorphic
829 transition and virulence of the human pathogenic zygomycete *Mucor*
830 *circinelloides*. PLoS Pathog. 2013;9(9):e1003625. pmid: 24039585.
831 29. Bastidas RJ, Shertz CA, Lee SC, Heitman J, Cardenas ME. Rapamycin exerts
832 antifungal activity in vitro and in vivo against *Mucor circinelloides v*ia FKBP12-
833 dependent inhibition of Tor. Eukaryot Cell. 2012;11(3):270-81. pmid: 22210828.
834 30. Navarro-Mendoza MI, Perez-Arques C, Heitman J. Heterochromatin and RNAi
835 act independently to ensure genome stability in Mucorales human fungal
836 pathogens. Proc Natl Acad Sci U S A. 2023;120(7):e2220475120. pmid:
837 36745785.
838 31. Huang J, Larmore CJ, Priest SJ, Xu Z, Dietrich FS, Yadav V, et al. Distinct
839 evolutionary trajectories following loss of RNA interference in *Cryptococcus*

840 *neoformans*. Proc Natl Acad Sci U S A. 2024;121(47):e2416656121. pmid:
841 39536081.
842 32. Mi S, Cai T, Hu Y, Chen Y, Hodges E, Ni F, et al. Sorting of small RNAs into
843 *Arabidopsis* argonaute complexes is directed by the 5' terminal nucleotide. Cell.
844 2008;133(1):116-27. pmid: 18342361.
845 33. Bhattacharjee S, Roche B, Martienssen RA. RNA-induced initiation of
846 transcriptional silencing (RITS) complex structure and function. RNA Biol.
847 2019;16(9):1133-46. pmid: 31213126.
848 34. Allshire RC, Madhani HD. Ten principles of heterochromatin formation and
849 function. Nat Rev Mol Cell Biol. 2018;19(4):229-44. pmid: 29235574.
850 35. Filipowicz W, Jaskiewicz L, Kolb FA, Pillai RS. Post-transcriptional gene silencing
851 by siRNAs and miRNAs. Curr Opin Struct Biol. 2005;15(3):331-41. pmid:
852 15925505.
853 36. Chang Z, Heitman J. Drug-resistant epimutants exhibit organ-specific stability
854 and induction during murine infections caused by the human fungal pathogen
855 *Mucor circinelloides*. mBio. 2019;10(6):e02579-19. pmid: 31690679.
856 37. Rhodes J, Abdolrasouli A, Farrer RA, Cuomo CA, Aanensen DM, Armstrong-
857 James D, et al. Genomic epidemiology of the UK outbreak of the emerging
858 human fungal pathogen *Candida auris*. Emerg Microbes Infect. 2018;7(1):43.
859 pmid: 29593275.
860 38. Fraaije B, Atkins S, Hanley S, Macdonald A, Lucas J. The multi-fungicide
861 resistance status of *Aspergillus fumigatus* populations in arable soils and the
862 wider European environment. Front Microbiol. 2020;11:599233. pmid: 33384673.
863 39. Ikuta KS, Mestrovic T, Naghavi M. Global incidence and mortality of severe
864 fungal disease. Lancet Infect Dis. 2024;24(5):e268. pmid: 38395046.
865 40. Park HS, Lee SC, Cardenas ME, Heitman J. Calcium-calmodulin-calcineurin
866 signaling: A globally conserved virulence cascade in eukaryotic microbial
867 pathogens. Cell Host Microbe. 2019;26(4):453-62. pmid: 31600499.
868 41. Trivedi P, Leach JE, Tringe SG, Sa T, Singh BK. Plant-microbiome interactions:
869 from community assembly to plant health. Nat Rev Microbiol. 2020;18(11):607-
870 21. pmid: 32788714.
871 42. Faust K, Raes J. Microbial interactions: from networks to models. Nat Rev
872 Microbiol. 2012;10(8):538-50. pmid: 22796884.
873 43. Weiland-Brauer N. Friends or Foes-Microbial Interactions in Nature. Biology
874 (Basel). 2021;10(6). pmid: 34199553.
875 44. Getzke F, Thiergart T, Hacquard S. Contribution of bacterial-fungal balance to
876 plant and animal health. Curr Opin Microbiol. 2019;49:66-72. pmid: 31731228.
877 45. de Menezes AB, Richardson AE, Thrall PH. Linking fungal-bacterial co-
878 occurrences to soil ecosystem function. Curr Opin Microbiol. 2017;37:135-41.
879 pmid: 28692866.
880 46. Baumgardner DJ. Soil-related bacterial and fungal infections. J Am Board Fam
881 Med. 2012;25(5):734-44. pmid: 22956709.
882 47. Procopio RE, Silva IR, Martins MK, Azevedo JL, Araujo JM. Antibiotics produced
883 by *Streptomyces*. Braz J Infect Dis. 2012;16(5):466-71. pmid: 22975171.
884 48. Kino T, Hatanaka H, Hashimoto M, Nishiyama M, Goto T, Okuhara M, et al. FK-
885 506, a novel immunosuppressant isolated from a *Streptomyces*. I. Fermentation,

886 isolation, and physico-chemical and biological characteristics. J Antibiot (Tokyo).
887 1987;40(9):1249-55. pmid: 2445721.
888 49. Arndt C, Cruz MC, Cardenas ME, Heitman J. Secretion of FK506/FK520 and
889 rapamycin by *Streptomyces* inhibits the growth of competing *Saccharomyces*
890 *cerevisiae* and *Cryptococcus neoformans*. Microbiology (Reading). 1999;145 (Pt
891 8):1989-2000. pmid: 10463165.
892 50. Ziaee A, Zia M, Bayat M, Hashemi J. Identification of Mucorales isolates from soil
893 using morphological and molecular methods. Curr Med Mycol. 2016;2(1):13-9.
894 pmid: 28681007.
895 51. Abu-Salah KM. Amphotericin B: an update. Br J Biomed Sci. 1996;53(2):122-33.
896 pmid: 8757689.
897 52. Nicolas FE, Torres-Martinez S, Ruiz-Vazquez RM. Two classes of small
898 antisense RNAs in fungal RNA silencing triggered by non-integrative transgenes.
899 EMBO J. 2003;22(15):3983-91. pmid: 12881432.
900 53. Calo S, Nicolas FE, Lee SC, Vila A, Cervantes M, Torres-Martinez S, et al. A
901 non-canonical RNA degradation pathway suppresses RNAi-dependent
902 epimutations in the human fungal pathogen *Mucor circinelloides*. PLoS Genet.
903 2017;13(3):e1006686. pmid: 28339467.
904 54. Nicolas FE, Moxon S, de Haro JP, Calo S, Grigoriev IV, Torres-Martinez S, et al.
905 Endogenous short RNAs generated by Dicer 2 and RNA-dependent RNA
906 polymerase 1 regulate mRNAs in the basal fungus *Mucor circinelloides*. Nucleic
907 Acids Res. 2010;38(16):5535-41. pmid: 20427422.
908 55. Brodersen P, Voinnet O. The diversity of RNA silencing pathways in plants.
909 Trends Genet. 2006;22(5):268-80. pmid: 16567016.
910 56. Hamilton A, Voinnet O, Chappell L, Baulcombe D. Two classes of short
911 interfering RNA in RNA silencing. EMBO J. 2015;34(20):2590. pmid: 26291654.
912 57. Chakravarthy S, Sternberg SH, Kellenberger CA, Doudna JA. Substrate-specific
913 kinetics of Dicer-catalyzed RNA processing. J Mol Biol. 2010;404(3):392-402.
914 pmid: 20932845.
915 58. Vermeulen A, Behlen L, Reynolds A, Wolfson A, Marshall WS, Karpilow J, et al.
916 The contributions of dsRNA structure to Dicer specificity and efficiency. RNA.
917 2005;11(5):674-82. pmid: 15811921.
918 59. Djupedal I, Ekwall K. Epigenetics: heterochromatin meets RNAi. Cell Res.
919 2009;19(3):282-95. pmid: 19188930.
920 60. Okazaki K, Kato H, Iida T, Shinmyozu K, Nakayama JI, Murakami Y, et al. RNAi-
921 dependent heterochromatin assembly in fission yeast S*chizosaccharomyces*
922 *pombe* requires heat-shock molecular chaperones Hsp90 and Mas5. Epigenetics
923 Chromatin. 2018;11(1):26. pmid: 29866182.
924 61. Bayne EH, White SA, Kagansky A, Bijos DA, Sanchez-Pulido L, Hoe KL, et al.
925 Stc1: a critical link between RNAi and chromatin modification required for
926 heterochromatin integrity. Cell. 2010;140(5):666-77. pmid: 20211136.
927 62. Yu R, Wang X, Moazed D. Epigenetic inheritance mediated by coupling of RNAi
928 and histone H3K9 methylation. Nature. 2018;558(7711):615-9. pmid: 29925950.
929 63. Funannotate v1.8.1: Eukaryotic genome annotation [Internet]. Zenodo. 2020.

930 64. Koren S, Walenz BP, Berlin K, Miller JR, Bergman NH, Phillippy AM. Canu:
931 scalable and accurate long-read assembly via adaptive k-mer weighting and
932 repeat separation. Genome Res. 2017;27(5):722-36. pmid: 28298431.
933 65. Kolmogorov M, Yuan J, Lin Y, Pevzner PA. Assembly of long, error-prone reads
934 using repeat graphs. Nat Biotechnol. 2019;37(5):540-6. pmid: 30936562.
935 66. Son YE, Yu JH, Park HS. The novel spore-specific regulator SscA controls
936 *Aspergillus* conidiogenesis. mBio. 2023;14(5):e0184023. pmid: 37707170.
937 67. Bushnell B. BBMap: A fast, accurate, splice-aware aligner. 2014.
938 68. Li H, Handsaker B, Wysoker A, Fennell T, Ruan J, Homer N, et al. The
939 Sequence Alignment/Map format and SAMtools. Bioinformatics.
940 2009;25(16):2078-9. pmid: 19505943.
941 69. Priest SJ, Yadav V, Roth C, Dahlmann TA, Kuck U, Magwene PM, et al.
942 Uncontrolled transposition following RNAi loss causes hypermutation and
943 antifungal drug resistance in clinical isolates of *Cryptococcus neoformans*. Nat
944 Microbiol. 2022;7(8):1239-51. pmid: 35918426.
945 70. Park HS, Man Yu Y, Lee MK, Jae Maeng P, Chang Kim S, Yu JH. Velvet-
946 mediated repression of beta-glucan synthesis in *Aspergillus nidulans* spores. Sci
947 Rep. 2015;5:10199. pmid: 25960370.
948 71. Navarro-Mendoza MI, Perez-Arques C, Panchal S, Nicolas FE, Mondo SJ,
949 Ganguly P, et al. Early diverging fungus *Mucor circinelloides* lacks centromeric
950 histone CENP-A and displays a mosaic of point and regional centromeres. Curr
951 Biol. 2019;29(22):3791-802 e6. pmid: 31679929.
952 72. Bolger AM, Lohse M, Usadel B. Trimmomatic: a flexible trimmer for Illumina
953 sequence data. Bioinformatics. 2014;30(15):2114-20. pmid: 24695404.
954 73. Langmead B, Salzberg SL. Fast gapped-read alignment with Bowtie 2. Nat
955 Methods. 2012;9(4):357-9. pmid: 22388286.
956 74. Zhang Y, Liu T, Meyer CA, Eeckhoute J, Johnson DS, Bernstein BE, et al.
957 Model-based analysis of ChIP-Seq (MACS). Genome Biol. 2008;9(9):R137.
958 pmid: 18798982.
959 75. Ramirez F, Dundar F, Diehl S, Gruning BA, Manke T. deepTools: a flexible
960 platform for exploring deep-sequencing data. Nucleic Acids Res. 2014;42:W187-
961 91. pmid: 24799436.
962 76. Robinson JT, Thorvaldsdottir H, Turner D, Mesirov JP. igv.js: an embeddable
963 JavaScript implementation of the Integrative Genomics Viewer (IGV).
964 Bioinformatics. 2023;39(1). pmid: 36562559.
965

966 **Figure legends**

967 **Fig 1. FK506-resistant strains isolated from the *Mucor circinelloides* complex.**

968 **(A)** Schematic representation of the procedure followed to obtain FK506- and/or
969 rapamycin-resistant strains from *Mucor circinelloides* complex species. This Figure was
970 generated with BioRender.com. **(B)** Phenotypic analysis of FK506-resistant isolates in *M.*
971 *janssenii* CBS185.68 (PS1), *M. bainieri* CBS293.63 (PS3), and *M. atramentarius*
972 CBS202.28 (PS6). WT, wild-type; M, Mendelian mutant; E, Epimutant.

973

974 **Fig 2. FK506-resistant epimutants exhibit silencing of *fkbA* mRNA and FKBP12**
975 **protein expression and are unstable.**

976 **(A, D)** Phenotypic reversion of FK506-resistant epimutant strains following serial passage
977 without drug selection in *M. bainieri* (A) or *M. atramentarius* (D). Red arrows indicate the
978 points at which epimutants reverted to the WT phenotype. FK506 was utilized at 1 µg/mL
979 and rapamycin at 100 ng/mL. WT, wild-type; P, number of passages. **(B, E)** Quantification
980 of the *fkbA* mRNA expression in *M. bainieri* (B) *or M. atramentarius* (E). Error bars
981 represent mean ± SEM (n = 3). Statistical significance: $^{****}p \leq 0.0001$. **(C, F)** Western blot
982 analysis of FKBP12 protein expression in *M. bainieri* (C) or *M. atramentarius* (F). PS3:
983 E1–E9, epimutants; E1P4–E9P24, revertants. PS6: E1 and E2, epimutants; E1P32 and
984 E2P28, revertants.

985 **Fig 3. Small RNAs mediate FK506 resistance in *M. bainieri*.**

986 **(A)** Small RNA coverage mapped across the *fkbA* gene and its neighboring loci. The right
987 panel presents a detailed view of the *fkbA* gene and its neighboring loci. Peaks shown
988 below the coverage track indicate statistically enriched small RNA intervals identified by
989 the MACS3 peak-calling algorithm, which models background signal to detect significant
990 enrichment. **(B)** Small RNA abundance (RPM: reads per million) mapped to the *fkbA* gene.
991 **(C)** 5′-end nucleotide preference of small RNAs associated with the *fkbA* gene. **(D)** Size
992 distribution of small RNAs mapped to the *fkbA* gene. WT, wild-type; E1–E9, epimutants;
993 E1P4–E9P24, revertants.

994

995 **Fig 4. Heterochromatin marks underlie epigenetic FK506 resistance in *M. bainieri*.**

996 **(A)** ChIP-qPCR analysis of H3K9me2 enrichment at the positive control region (an siRNA-
997 enriched locus validated by H3K9me2) and *fkbA* locus (targeting the 5′-UTR, exonic
998 regions, and 3′-UTR). Error bars represent mean ± SEM (n = 3). Statistical significance:
999 $^{*}p \leq 0.05$, $^{**}p \leq 0.01$; $^{****}p \leq 0.0001$. **(B, C)** ChIP-seq coverage mapped across the positive
1000 control locus (an siRNA-enriched locus validated by H3K9me2; B) or *fkbA* and its
1001 neighboring loci (C). The peaks shown beneath the coverage track denote significant
1002 H3K9me2-enriched intervals identified by the MACS3 peak-calling algorithm, which
1003 detects statistically enriched regions by modeling background signal. **(D)** ChIP-qPCR
1004 analysis of RNA polymerase II enrichment at the positive control region (*actA*), *fkbA* locus
1005 (targeting the 5′-UTR and exonic region), a *fkbA*-neighboring gene, and negative control,
1006 defined as an siRNA-producing region flanked by transposable elements and associated

1007 with H3K9me2. Statistical significance: ****$p \leq 0.0001$. WT, wild-type; E1–E8, epimutants;
1008 E1P4–E8P28, revertants.
1009
1010 **Fig 5. Heterochromatin-associated FK506 resistance is conserved in *M.***
1011 ***atramentarius*.**
1012 **(A)** Small RNA coverage mapped across the *fkbA* gene and its neighboring loci. Below
1013 panel presents a detailed view of the *fkbA* gene and its neighboring loci. Peaks shown
1014 below the coverage track indicate statistically enriched small RNA intervals identified by
1015 the MACS3 peak-calling algorithm, which models background signal to detect significant
1016 enrichment. **(B)** ChIP-qPCR analysis of H3K9me2 enrichment at the the GremLINE1
1017 transposon (positive control region) and *fkbA* locus (targeting the 5′-UTR, exonic regions,
1018 and 3′-UTR). Error bars represent mean ± SEM (n = 3). Statistical significance: ****$p \leq$
1019 0.0001. **(C, D)** ChIP-seq coverage mapped across the GremLINE1 transposon and its
1020 neighboring loci (C) or *fkbA* and its neighboring loci (D). The peaks shown beneath the
1021 coverage track denote significant H3K9me2-enriched intervals identified by the MACS3
1022 peak-calling algorithm, which detects statistically enriched regions by modeling
1023 background signal. **(E)** ChIP-qPCR analysis of RNA polymerase II enrichment at the
1024 positive control region (*actA*), *fkbA* locus (targeting the 5′-UTR and exonic region), a *fkbA*-
1025 neighboring gene, and negative control locus, defined as an siRNA-producing region
1026 flanked by transposable elements and associated with H3K9me2. Statistical significance:
1027 ****$p \leq 0.0001$. WT, wild-type; E1 and E2, epimutants; E1P32 and E2P28, revertants.
1028

1029 **Fig 6. Inherited heterochromatin-mediated antifungal resistance persists after *in***
1030 ***vivo* passage.**
1031 **(A)** Fungal growth of *M. circinelloides*, *M. bainieri* and *M. atramentarius* under different
1032 temperature conditions. Microscopic images show enlarged sporangia (scale bar =
1033 20 μm). **(B)** Survival rates of mice infected with *M. atramentarius*. *Mucor circinelloides*
1034 and PBS served as positive and negative controls, respectively. The log-rank test
1035 revealed a statistically significant difference in survival between groups (*M. atramentarius*
1036 vs PBS, $p = 0.014$). **(C)** Fungal colonies recovered from four different organs following *in*
1037 *vivo* infection with wild-type (WT), epimutant (E1), and revertant (E1P32) strains. The bar
1038 plot (right) shows the percentage of FK506-resistant colonies from each organ after
1039 passage. **(D)** ChIP-qPCR analysis of H3K9me2 enrichment at the *fkbA* locus following *in*
1040 *vivo* passage, targeting two exonic regions. Error bars represent mean ± SEM (n = 3).
1041 Statistical significance: $^{****}p \leq 0.0001$. WT, wild-type; E1R1–E1R3, FK506-resistant
1042 epimutants; E1S1, FK506-sensitive epimutant; E1P32, revertant.
1043
1044 **Fig 7. Heterochromatin-mediated antifungal resistance remains stable after *in vivo***
1045 **infection in immunosuppressed and non-immunosuppressed mice.**
1046 **(A−C)** Fungal colonies recovered from four different organs following *in vivo* infection with
1047 heterochromatin-mediated epimutant under three different conditions: (A)
1048 cyclophosphamide-treated mice (50 mg/kg, 2 weeks post-infection), (B) untreated mice
1049 (2 weeks post-infection), and (C) untreated mice (4 weeks post-infection). The right bar
1050 plot shows the percentage of FK506-resistant colonies recovered from each organ under
1051 each condition. **(D−F)** ChIP-qPCR analysis of H3K9me2 enrichment at the *fkbA* locus

1052 under the same three conditions: (D) cyclophosphamide-treated mice (50 mg/kg, 2 weeks
1053 post-infection), (E) untreated mice (2 weeks post-infection), and (F) untreated mice (4
1054 weeks post-infection). Error bars represent mean ± SEM (n = 3). Statistical significance:
1055 $^{**}p \leq 0.01$; $^{****}p \leq 0.0001$.
1056
1057 **Fig 8. Schematic overview of epigenetic genetic silencing contributing to antifungal**
1058 **resistance in *Mucor* species.**
1059 *fkbA* expression enables FKBP12 production and FK506 sensitivity (yeast-like
1060 morphology). Epigenetic silencing of *fkbA* via RNAi or heterochromatin leads to FK506
1061 resistance and hyphal growth. Generated with BioRender.com.

1062 **Table 1. FK506 resistant strains isolated in this study.**

Species	Name	Phenotype	*fkbA* mutation	Impact on FKBP12	Calcineurin mutation
PS1 *Mucor janssenii*	M1	FK506-R, Rapa-S	No	No	G1496C in *cnaA* (G347A missense mutation)
	M2	FK506-R, Rapa-R	4,324 bp insertion (Unknown) at 38 bp upstream *fkbA* ORF	-	-
	M3	FK506-R, Rapa-R	Large deletion	Loss	-
	M4	FK506-R, Rapa-R	Large deletion	Loss	-
	M5	FK506-R, Rapa-R	5,052 bp insertion (RC/Helitron_DNA transposons) at 16 bp upstream *fkbA* ORF	-	-
	M6	FK506-R, Rapa-R	C120 1 bp deletion in exon 2 (Frameshift)	Nonsense mutation	-
	M7	FK506-R, Rapa-R	Large deletion	Loss	-
	M8	FK506-R, Rapa-R	G258C in 5' splice site of intron2	-	-
	M9	FK506-R, Rapa-R	Large deletion	Loss	-
	M10	FK506-R, Rapa-R	G258C in 5' splice site of intron2	-	-
PS3 *Mucor bainieri*	E1	FK506-R, Rapa-R	No	No	No
	E2	FK506-R, Rapa-R	No	No	No
	E3	FK506-R, Rapa-R	No	No	No
	E4	FK506-R, Rapa-R	No	No	No
	E5	FK506-R, Rapa-R	No	No	No
	E6	FK506-R, Rapa-R	No	No	No
	M1	FK506-R, Rapa-R	C357 1 bp deletion in exon 3 (Frameshift)	Nonsense mutation	No
	E7	FK506-R, Rapa-R	No	No	No
	E8	FK506-R, Rapa-R	No	No	No
	E9	FK506-R, Rapa-R	No	No	No

PS6 *Mucor atramentarius*	M1	FK506-R, Rapa-R	C404 1 bp deletion in exon 3 (Frameshift)	Nonsense mutation	No
	M2	FK506-R, Rapa-S	No	No	G477T in *cnbR* (V122F missense mutation)
	M3	FK506-R, Rapa-R	G249A in 5′ splice site	No	No
	M4	FK506-R, Rapa-R	G249A in 5′ splice site	No	No
	M5	FK506-R, Rapa-S	G189T in exon 2	Synonymous mutation	No
	M6	FK506-R, Rapa-R	C404 1 bp deletion in exon 3 (Frameshift)	Nonsense mutation	No
	M7	FK506-R, Rapa-R	T2C in exon 1 (start-loss mutation)	Loss	No
	E1	FK506-R, Rapa-R	No	No	No
	E2	FK506-R, Rapa-R	No	No	No
	M8	FK506-R, Rapa-R	C404 1 bp deletion in exon 3 (Frameshift)	Nonsense mutation	No

1063

1064 **Table 2. Epimutant reverted strains analyzed in this study.**

Species	Name	Background	Phenotype	Description
PS3 *Mucor bainieri*	E1P4	E1	FK506-S, Rapa-S	E1 Revertant after passage 4
	E2P4	E2	FK506-S, Rapa-S	E2 Revertant after passage 4
	E3P12	E3	FK506-S, Rapa-S	E3 Revertant after passage 12
	E3P16	E4	FK506-S, Rapa-S	E4 Revertant after passage 16
	E5P12	E5	FK506-S, Rapa-S	E5 Revertant after passage 12
	E6P12	E6	FK506-S, Rapa-S	E6 Revertant after passage 12
	E7P28	E7	FK506-S, Rapa-S	E7 Revertant after passage 28
	E8P28	E8	FK506-S, Rapa-S	E8 Revertant after passage 28
	E9P24	E9	FK506-S, Rapa-S	E9 Revertant after passage 24
PS6 *Mucor atramentarius*	E1P32	E1	FK506-S, Rapa-S	E1 Revertant after passage 32
	E2P28	E2	FK506-S, Rapa-S	E2 Revertant after passage 28

1065

1066 **Table 3. Summary of epigenetic mechanisms in *Mucor bainieri*.**

Type	Mechanisms	Epimutant	Revertant	Average passages for revertant
1	RNAi-associated heterochromatin-dependent silencing	E1	E1P4	6.67
		E2	E2P4	
		E3	E3P12	
2	Heterochromatin-dependent silencing	E4	E3P16	16
3	Canonical RNAi-dependent silencing	E5	E5P12	18.8
		E6	E6P12	
		E7	E7P28	
		E8	E8P28	
		E9	E9P24	

1067

Figure 1. Son et al.

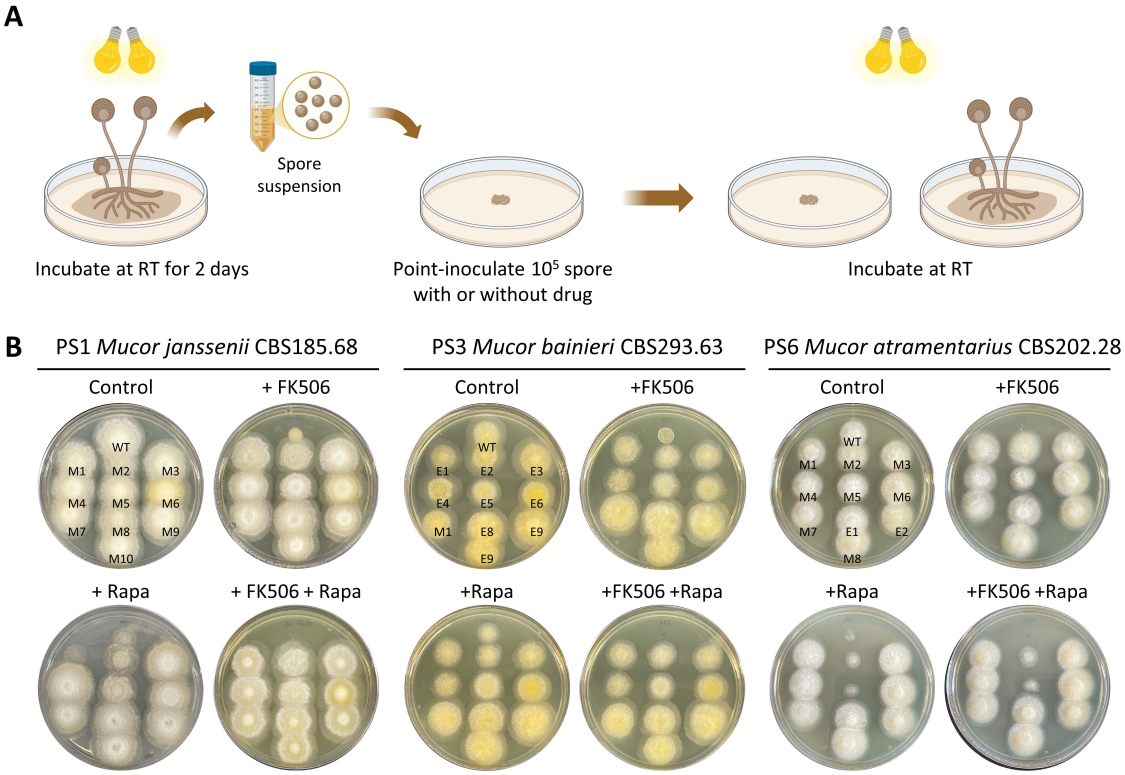

Figure 2. Son et al.

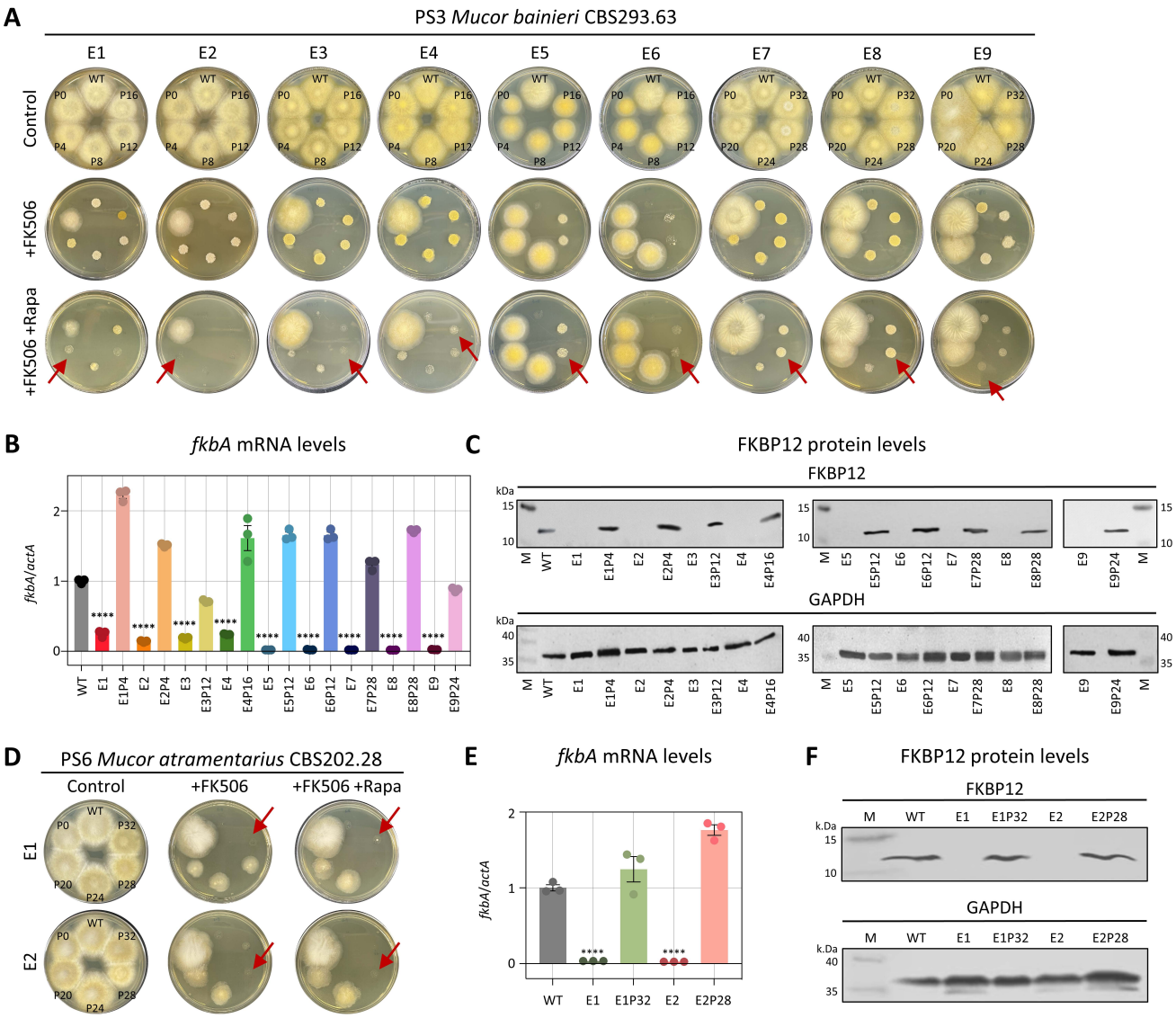

Figure 3. Son et al.

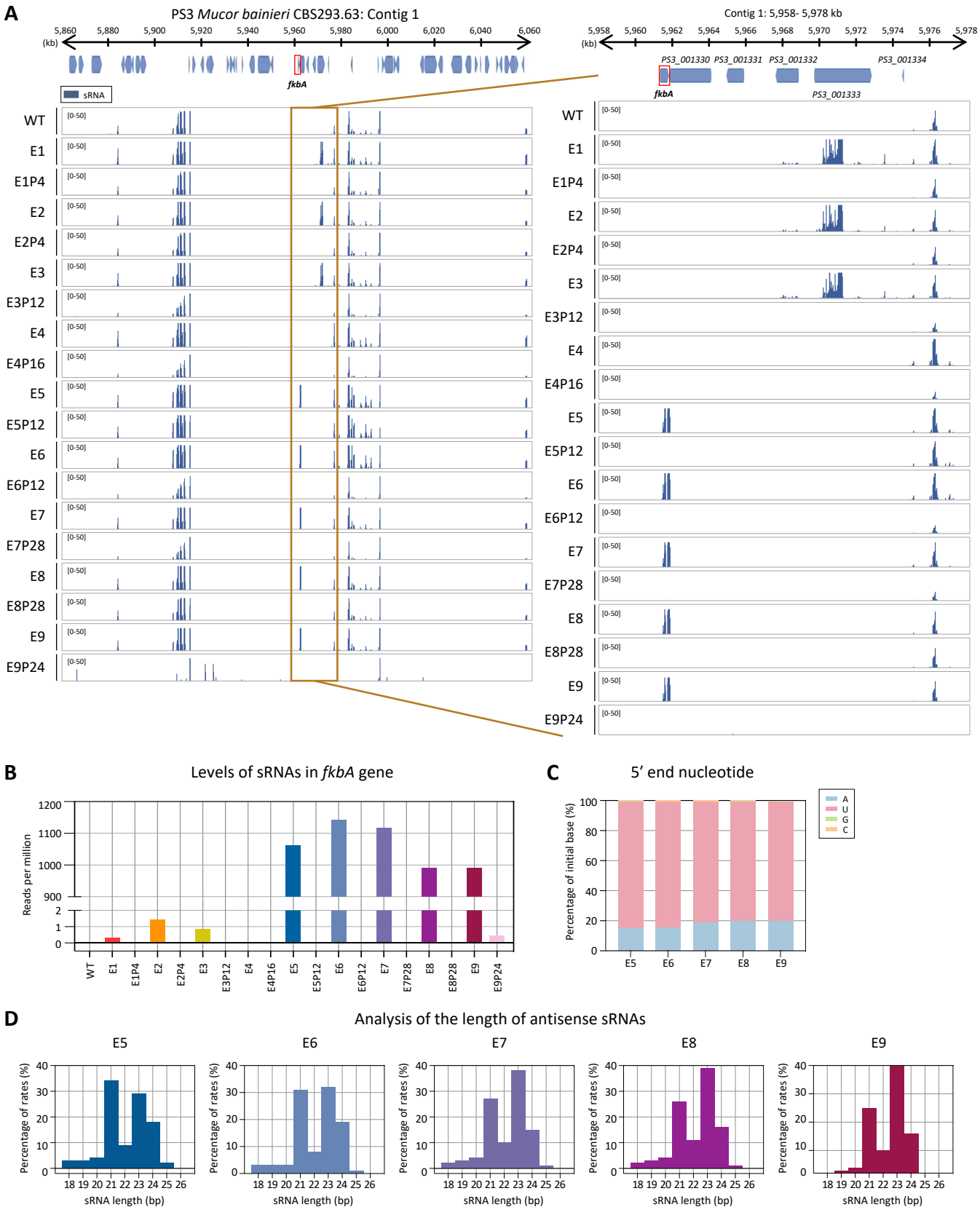

Figure 4. Son et al.

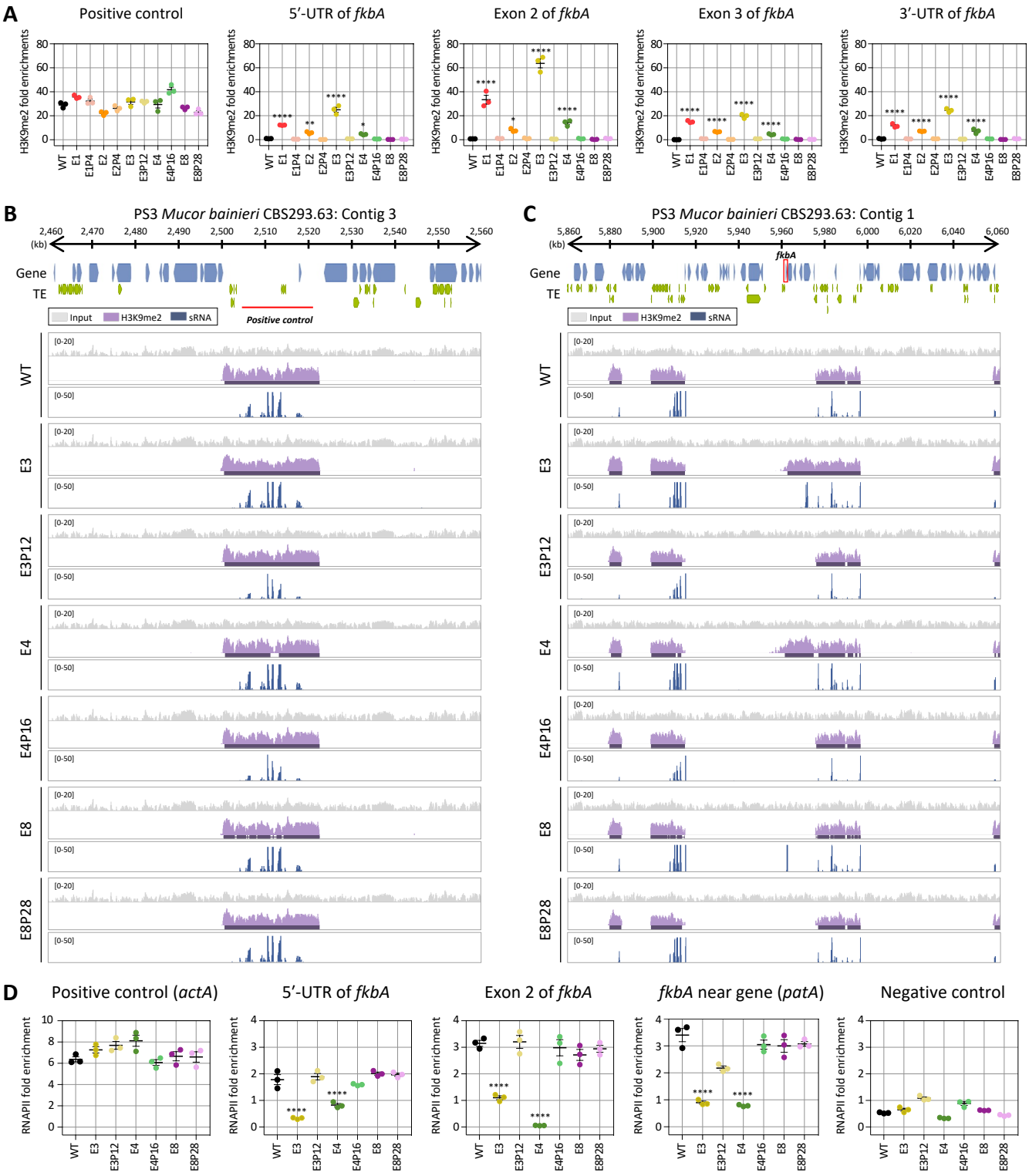

Figure 5. Son et al.

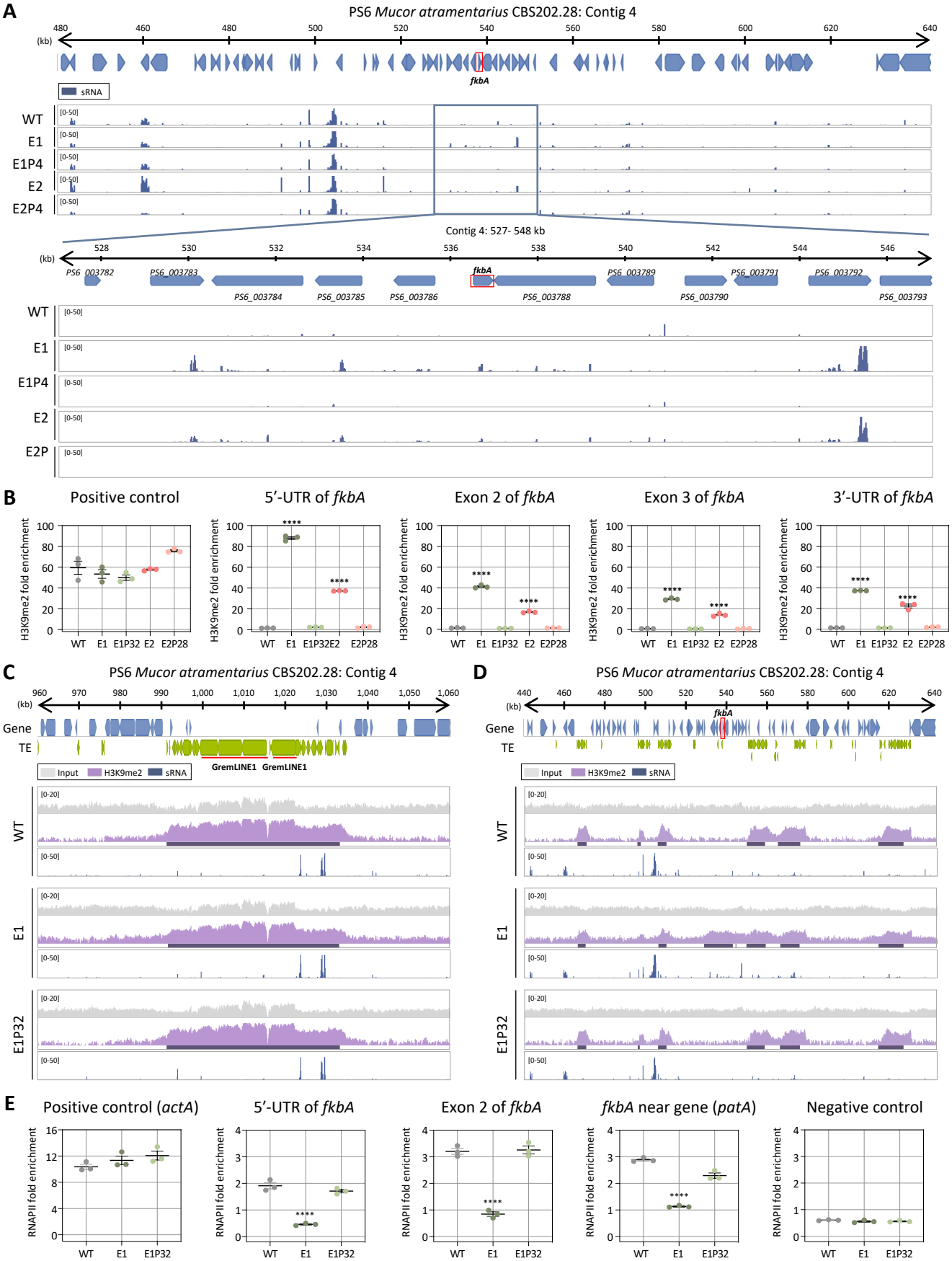

Figure 6. Son et al.

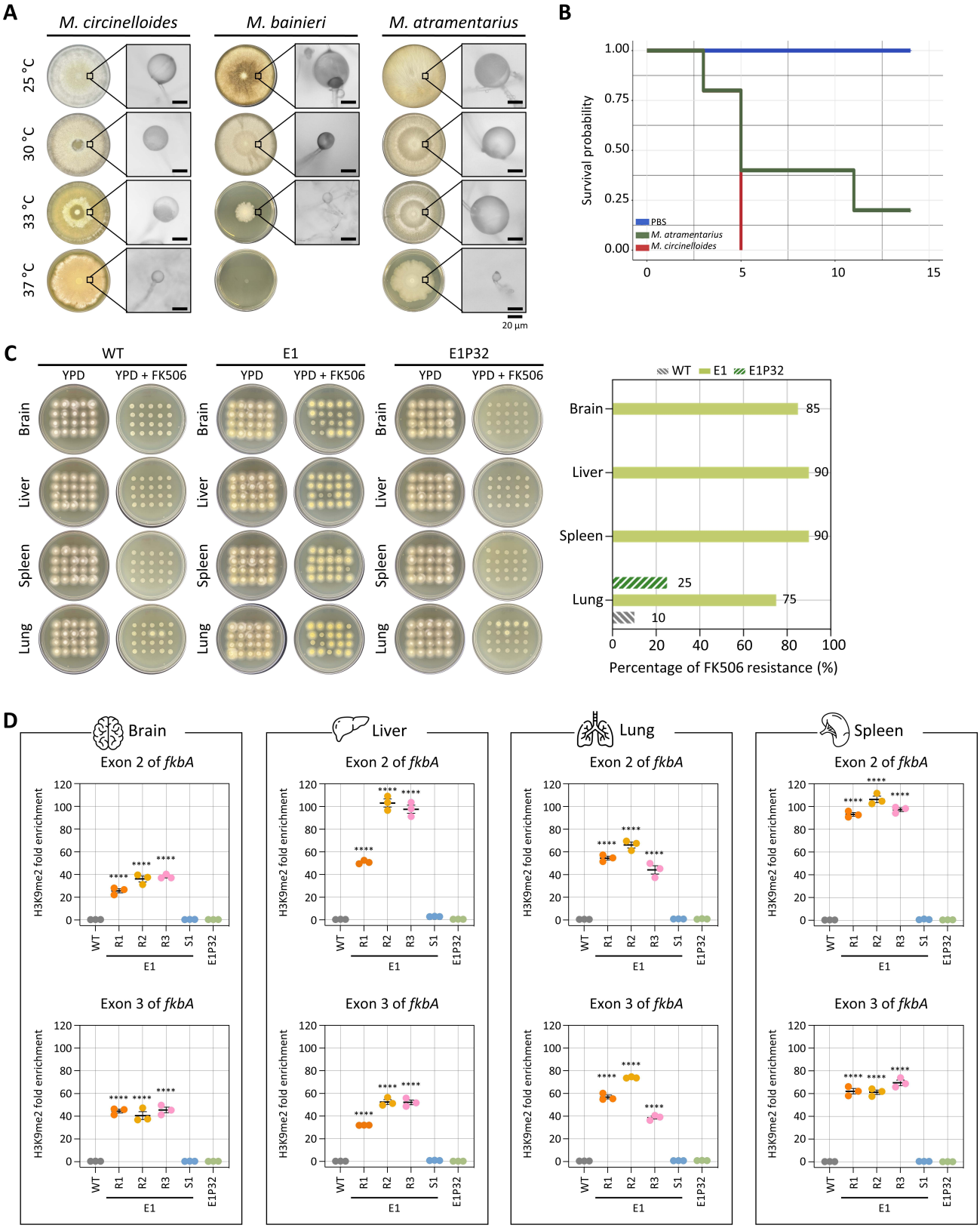

Figure 7. Son et al.

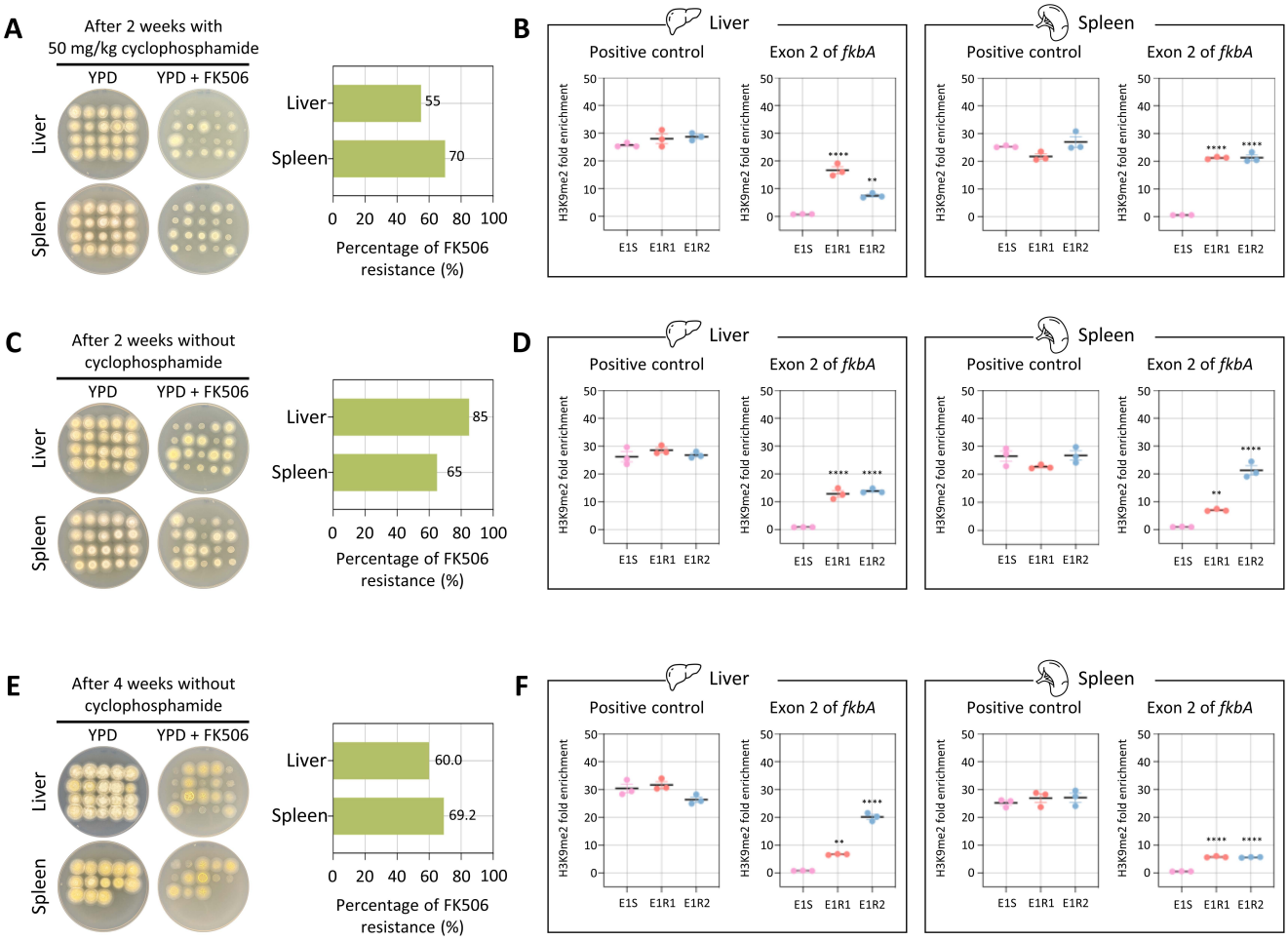
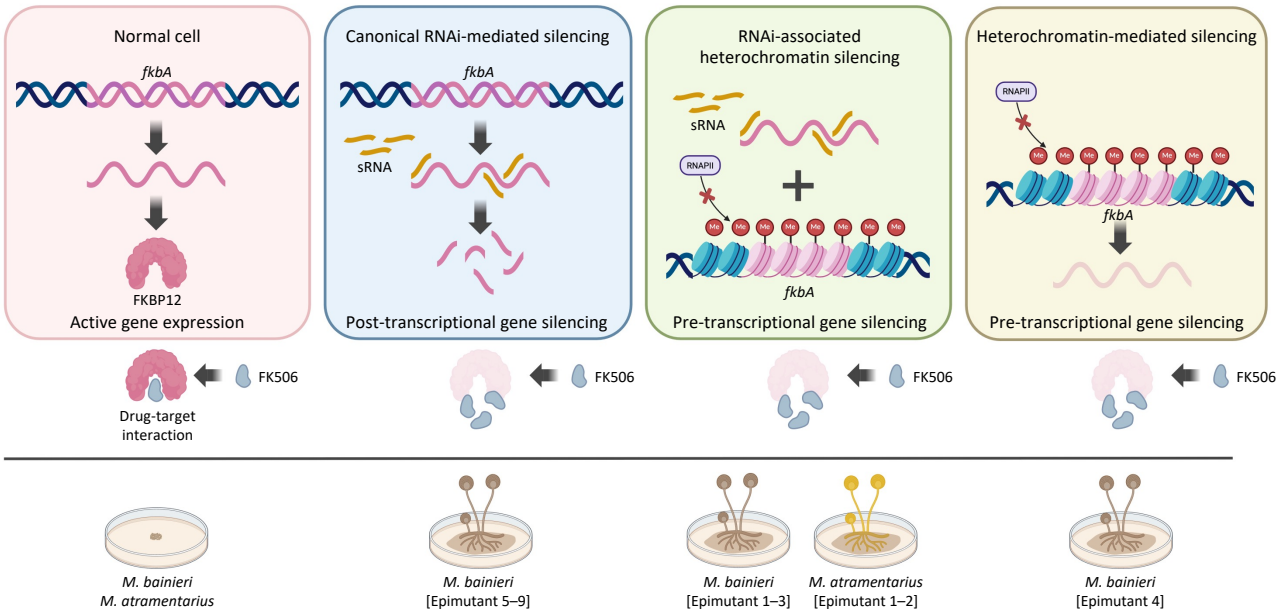
Figure 8. Son et al.